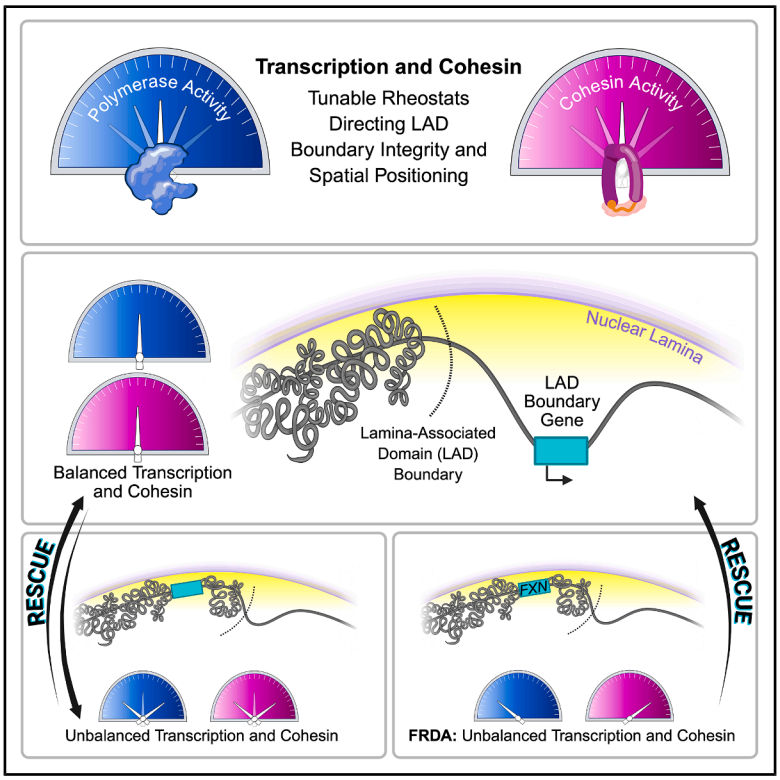
Molecular Cell

Article

Transcription and cohesin direct domain boundary spatial positioning and are linked to Friedreich's ataxia

Graphical abstract



Highlights

- A transcription-cohesin rheostat tunes LAD-boundary gene proximity to the lamina
- Repression drives boundary genes to the lamina in a cohesin-dependent manner
- Forced transcription opposes cohesin-driven peripheral repositioning of boundary genes
- In FRDA, re-tuning by reducing cohesin repositions *FXN* and partially rescues expression

Authors

Ashley Karnay,
Ricardo Linares-Saldana,
Qiaohong Wang, ...,
Melike Lakadamyali, Eric F. Joyce,
Rajan Jain

Correspondence

jainr@pennmedicine.upenn.edu

In brief

Karnay et al. reveal a tunable balance between transcription and cohesin that controls whether genomic regions reside at the nuclear periphery. By modulating transcription and cohesin activity, this balance can be shifted to alter gene positioning, including in Friedreich's ataxia (FRDA), where reducing cohesin partially restores *FXN* positioning and expression.

Karnay et al., 2026, Molecular Cell *86*, 1911–1930
May 21, 2026 © 2026 The Authors. Published by Elsevier Inc.
https://doi.org/10.1016/j.molcel.2026.04.019

CellPress

Molecular Cell

CellPress
OPEN ACCESS

Article

Transcription and cohesin direct domain boundary spatial positioning and are linked to Friedreich's ataxia

Ashley Karnay,[1,2] Ricardo Linares-Saldana,[1,2] Qiaohong Wang,[1,2] Zachary Gardner,[1,2] Jialiu A. Liang,[1,2] Garrett T. Santini,[1,2] Krishna Kumar Haridhasapavalan,[1,2] Son C. Nguyen,[2,3] Siewert Hugelier,[4] Bhavana Shewale,[5] Masato T. Kanemaki,[6,7,8] Jill S. Napierala,[9] Marek Napierala,[9] Robert B. Wilson,[10] Nicole Dubois,[5] Andrey Poleshko,[1,2] Wonho Kim,[1,2,11] Parisha P. Shah,[1,2] Melike Lakadamyali,[2,4] Eric F. Joyce,[2,3] and Rajan Jain[1,2,12,13,*]

[1]Department of Cell and Developmental Biology, Perelman School of Medicine, University of Pennsylvania, Philadelphia, PA 19104, USA
[2]Epigenetics Institute, Pereleman School of Medicine, University of Pennsylvania, Philadelphia, PA 19104, USA
[3]Department of Genetics, Perelman School of Medicine, University of Pennsylvania, Philadelphia, PA 19104, USA
[4]Department of Physiology, Perelman School of Medicine, University of Pennsylvania, Philadelphia, PA 19104, USA
[5]Department of Cell, Developmental and Regenerative Biology, Icahn School of Medicine at Mount Sinai, New York, NY 10029, USA
[6]Department of Biological Sciences, Graduate School of Science, National Institute of Genetics, Research Organization of Information and Systems (ROIS), Mishima, Shizuoka 411-8540, Japan
[7]Graduate Institute for Advanced Studies, SOKENDAI, Mishima, Shizuoka 411-8540, Japan
[8]Department of Biological Science, The University of Tokyo, Bunkyo-ku, Tokyo 113-0033, Japan
[9]Department of Neurology, Peter O'Donnell Jr. Brain Institute, University of Texas Southwestern Medical Center, Dallas, TX 75390, USA
[10]Department of Pathology and Laboratory Medicine, Penn/CHOP Center of Excellence for Friedreich's Ataxia Research, Children's Hospital of Philadelphia, Philadelphia, PA 19104, USA
[11]Department of Genetics, Integrative Program for Biological and Genome Sciences, University of North Carolina, Chapel Hill, NC 27599, USA
[12]Department of Medicine, Penn Cardiovascular Institute, Institute of Regenerative Medicine, Perelman School of Medicine, University of Pennsylvania, Philadelphia, PA 19104, USA
[13]Lead contact
*Correspondence: jainr@pennmedicine.upenn.edu
https://doi.org/10.1016/j.molcel.2026.04.019

SUMMARY

Variability in genome organization drives differential gene expression and shapes cellular diversity, yet whether transcription actively instructs genome structure and how this relationship is exploited in disease remains unclear. We show that transcription and cohesin direct the spatial positioning of lamina-associated domain (LAD) boundary genes. Transcriptional repression repositions LAD boundary genes to the nuclear lamina in a cohesin loop extrusion-dependent manner. Conversely, overactive cohesin is sufficient to reposition and silence LAD boundary genes, an effect counteracted by maintaining transcription. In Friedreich's ataxia, we demonstrate improper positioning of the pathogenically repressed LAD boundary gene *FRATAXIN* (*FXN*) at the nuclear periphery reflects an imbalance between transcription and cohesin dynamics. Importantly, modulating either transcription or cohesin activity restores *FXN* positioning and reactivates expression. Our findings establish transcription and cohesin as tunable molecular rheostats orchestrating LAD boundary spatial positioning and reveal how the flexible and dynamic nature of genome architecture is hijacked in disease.

INTRODUCTION

The nuclear lamina is a protein network on the inner nuclear membrane that serves as a scaffold to facilitate spatial genome organization and shape chromatin topology. Chromatin regions spatially positioned at the nuclear lamina are referred to as lamina-associated domains (LADs). Changes in genome-lamina interactions correlate with lineage restriction, and disruptions to LAD organization or spatial positioning have been associated with disease.[1–6] Traditionally, LADs have been described as blocks of transcriptionally silent chromatin, representing a correlative link between peripheral positioning and transcriptional repression. However, whether transcription directly shapes LAD organization remains an open question. Prior studies probing LAD-lamina interactions have often leveraged highly engineered or global perturbations, limiting insights into the direct mechanisms by which LADs are spatially positioned under physiological conditions and leaving unresolved how

This is an open access article under the CC BY-NC-ND license (http://creativecommons.org/licenses/by-nc-nd/4.0/).

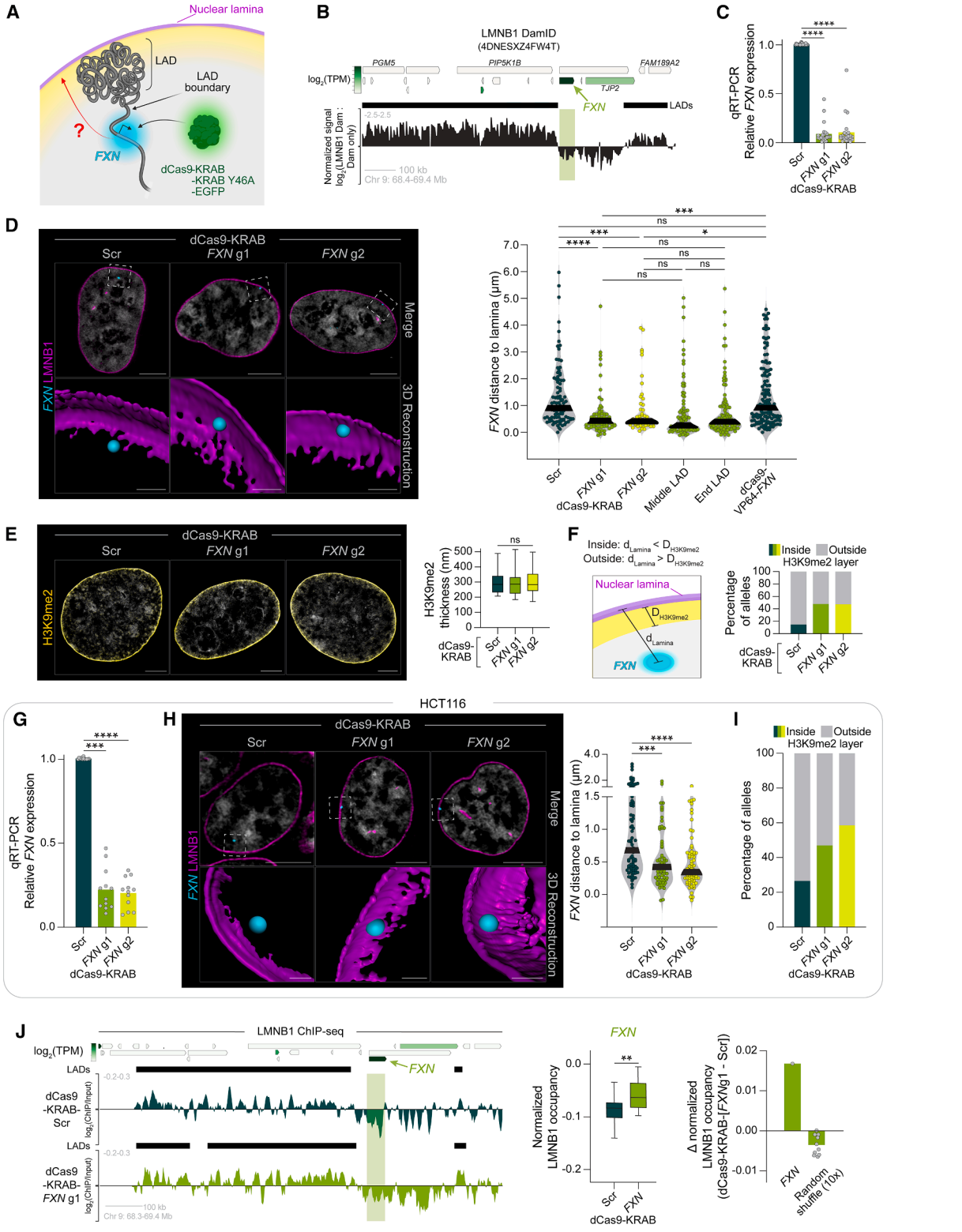


Figure 1. Transcriptional repression via CRISPRi repositions the LAD boundary gene *FXN* to the nuclear periphery

(A) Schematic illustrating dCas9+effector-mediated transcriptional repression of *FXN* and examination of *FXN* positioning relative to the nuclear periphery.

(B) LMNB1 DamID signal at *FXN* locus (HFFc6 fibroblasts, 4DNESXZ4FW4T). Black bars indicate LADs. Green color bar, expression of local genes (log_2TPM 0–3, RNA-seq, HFFc6). *FXN* locus highlighted.

(legend continued on next page)

transcription-lamina relationships contribute causally to disease. Notably, nonLAD genomic regions adjacent to LAD boundaries often harbor transcriptionally active genes.[7–10] Accordingly, LAD boundaries may represent unique regions whose regulation can be leveraged to elucidate whether and how transcription instructs genome spatial positioning.

Another level of chromatin topology comprises distinct structural units characterized by self-interaction, termed topologically associating domains (TADs).[11–15] TADs are regulated by the loop extrusion activity of the cohesin complex, a molecular motor that folds chromatin as it moves along the genome.[16–21] Although LADs and TADs represent distinct organizational units and are therefore often studied in isolation, a subset of LAD boundaries overlaps with TAD boundaries, and both boundary types are enriched in transcriptionally active genes.[22–24] These parallels suggest a potential interrelationship between the organizational principles governing these distinct facets of genome architecture; however, direct experimental evidence supporting such a link remains limited.

Changes in chromatin structure control gene expression, cell division, developmental progression, and intracellular responses to external cues.[25–33] However, the mechanisms driving structural flexibility remain poorly understood. Transcription is an attractive mechanism that may contribute to genome plasticity, as gene expression is inherently dynamic and can change in response to various factors, yet direct evidence that transcription shapes variation in 3D genome organization remains elusive. This gap is, in part, a consequence of prior studies' frequent reliance on global transcriptional inhibition and population-based assays. Furthermore, cohesin translocates along chromatin to dynamically sculpt genome structure, but whether and how cohesin activity is integrated with transcriptional state to contribute to organizational variability remains unclear. Defining the molecular drivers of genome structural variability is crucial for elucidating how changes in genome organization stem from molecular cues, influence cellular identity, and may be hijacked in disease.

Leveraging endogenous, locus-specific manipulations coupled with single-cell spatial measurements and genome-wide interrogations, we present a model underpinning LAD boundary plasticity in which transcriptional activity and cohesin dynamics act as tunable molecular rheostats that dictate LAD boundary spatial positioning. We further demonstrate that this mechanism contributes to the molecular pathology of Friedreich's ataxia (FRDA) and can be re-tuned to restore molecular pathology.

RESULTS

Targeted transcriptional repression repositions a LAD boundary gene to the nuclear periphery

To examine the relationship between LAD boundary gene expression and peripheral genome organization, we inhibited boundary gene transcription in a locus-specific manner and examined changes in target gene spatial positioning (Figure 1A). We mined Lamin B1 (LMNB1) DamID datasets from human fibroblasts and identified a model region that is locally depleted in LMNB1 occupancy, lies adjacent to a block of LMNB1-enriched chromatin, and contains an expressed gene (Figure 1B).[34,35] The *FXN* gene is located on chromosome 9 in humans, is expressed at approximately the 50th percentile of all expressed genes in human fibroblasts, and encodes the frataxin protein (FXN, Figure S1A).[36] To reduce *FXN* transcription, we introduced catalytically dead Cas9 fused to the KRAB repressive domain (dCas9-KRAB, CRISPRi) into immortalized human skin fibroblasts, with one of two guide RNAs (gRNAs) targeting the *FXN* promoter or transcriptional start site (g1 and g2, respectively; Figure S1B).[37] *FXN*-CRISPRi significantly reduced *FXN* transcript levels compared with a scramble, non-targeting gRNA (Scr-CRISPRi, Figure 1C). To assess the spatial positioning of *FXN* relative to the nuclear periphery, we measured the distance between the center of individual *FXN* alleles and the center of the nuclear lamina using 3D DNA fluorescent *in situ* hybridization (immunoDNA-FISH). *FXN* repositioned closer to the nuclear lamina in CRISPRi cells compared with Scr-CRISPRi controls (Figure 1D). To contextualize this shift, we compared *FXN* positioning with that of 20 individual LADs and nonLADs identified across 10 human cell types by LMNB1 ChIP-seq (Figure S1C).[9] In Scr-CRISPRi conditions, *FXN* was positioned farther from the nuclear periphery than the 20 LADs,

(C) *FXN* transcript levels in human fibroblasts expressing dCas9-KRAB and indicated gRNAs, normalized to Scr-CRISPRi. Bars represent means. Kruskal-Wallis test.

(D) (Left) Single-plane immunoDNA-FISH confocal images (top) with 3D reconstructions (bottom) showing *FXN* locus (cyan) and nuclear lamina (purple). Regions in dotted boxes are highlighted at the bottom. (Right) *FXN* positioning relative to nuclear lamina following transcriptional repression (dCas9-KRAB, CRISPRi) and transcriptional upregulation (dCas9-VP64, CRISPRa) and indicated regions. See STAR Methods. Kruskal-Wallis test.

(E) (Left) Confocal images of H3K9me2 immunostaining in the indicated conditions. (Right) Peripheral H3K9me2 thickness. Median and minimum/maximum. Kruskal-Wallis test.

(F) (Left) Schematic illustrating DNA-FISH loci stratification considered localized inside or outside peripheral chromatin if distance from the nuclear lamina (d_{Lamina}) is less than or greater than the H3K9me2 thickness ($D_{H3K9me2}$), respectively. (Right) Percentage of *FXN* alleles localized inside or outside the peripheral chromatin layer.

(G) *FXN* transcript levels in HCT116 in Scr- and *FXN*-CRISPRi, normalized to Scr-CRISPRi. Bars represent means. Kruskal-Wallis test.

(H) (Left) *FXN* immunoDNA-FISH images (top) with 3D reconstructions (bottom). (Right) *FXN* positioning relative to the lamina in HCT116 cells expressing Scr-CRISPRi or *FXN*-CRISPRi. Kruskal-Wallis test.

(I) Percentage of *FXN* alleles inside and outside of peripheral chromatin in indicated conditions (thickness quantified in Figure S1I).

(J) (Left) Input-normalized (log_2 ChIP/IP) LMNB1 ChIP-seq in Scr- and *FXN*-CRISPRi fibroblasts. Black bars indicate LADs. *FXN* locus highlighted. Green color bar, local gene expression levels (log_2TPM 0–3, RNA-seq, HFFc6). (Middle) Normalized *FXN* LMNB1 occupancy in Scr- and *FXN*-CRISPRi. Statistical comparisons across all 1 kb bins indicated by the green box, paired Wilcoxon signed-rank test. Effect size (r) = 0.431 (moderate, Rosenthal's r method). (Right) Delta mean normalized LMNB1 signal between Scr- and *FXN*-CRISPRi at *FXN* or 10,000 random regions matched for length and GC content (1,000 × 10). Scale bars: 5 and 1 μm (insets). Black bars on violin plots, medians.

but closer than the 20 nonLADs (Figure S1D). In contrast, CRISPRi-mediated repression repositioned *FXN* to distances comparable to those of two regions within the adjacent LAD (Figures 1D and S1C). Conversely, we forced *FXN* transcriptional upregulation by targeting the transcriptional activator VP64 fused to dCas9 (dCas9-VP64, CRISPRa).[38] *FXN*-CRISPRa resulted in an approximately 3-fold increase in transcript levels but did not lead to a significant change in *FXN* positioning relative to Scr-CRISPRa controls (Figures 1D and S1E). Collectively, these data define a zone in which *FXN* resides relative to the nuclear lamina in response to transcriptional repression or upregulation.

We and others have shown that LADs are enriched for dimethylation of lysine 9 on histone H3 (H3K9me2) and therefore use immunofluorescent H3K9me2 signal at the nuclear periphery as a measure of peripheral chromatin.[1,2,9,39] The average depth of H3K9me2-marked chromatin in Scr- versus *FXN*-CRISPRi cells was not statistically different (Figure 1E). Nearly 50% of *FXN* alleles were localized within the depth of H3K9me2-marked peripheral chromatin in *FXN*-CRISPRi cells, in contrast to 20% in Scr-CRISPRi control cells (Figure 1F), indicating that an approximate 30% shift in the fraction of *FXN* alleles at the periphery is associated with a significant reduction in transcription resulting from CRISPRi targeting. *FXN*-CRISPRi did not alter either the expression of *FXN*-adjacent genes or the spatial positioning of loci elsewhere on the same chromosome, supporting a specific effect of *FXN*-CRISPRi on *FXN* repositioning rather than a secondary consequence of broader disruptions in spatial organization (Figures S1F and S1G). Similar to fibroblasts, *FXN*-CRISPRi resulted in locus positioning closer to the nuclear periphery and increased association with H3K9me2-modified peripheral chromatin in HCT116 cells (Figures 1G–1I, S1H, and S1I). Thus, CRISPRi-mediated transcriptional repression leads to *FXN* repositioning to the nuclear peripheryin multiple cell types.

To examine changes in the chromatin-lamina landscape, we performed LMNB1 chromatin immunoprecipitation sequencing (ChIP-seq) in non-treated control (NTC), Scr-CRISPRi, and *FXN*-CRISPRi fibroblasts (Figures S1J and S1K). As expected, LADs were similar between NTC and Scr-CRISPRi and between Scr-CRISPRi and *FXN*-CRISPRi (Figures S1L and S1M). Furthermore, LADs identified in Scr-CRISPRi largely overlapped published human fibroblast LMNB1 DamID LADs (Figure S1M).[34] LMNB1 ChIP-seq in Scr-CRISPRi revealed *FXN* resides adjacent to a LAD (41 kb away) and is relatively devoid of LMNB1 occupancy (Figure 1J). In line with *FXN* peripheral repositioning observed by immunoDNA-FISH, *FXN* gained LMNB1 occupancy in *FXN*-CRISPRi compared with Scr-CRISPRi. This moderate increase was observed even when accounting for signal differences between the datasets at random genomic regions (Figure 1J). These results demonstrate that CRISPRi-associated *FXN* repositioning to the lamina is accompanied by a statistically significant increase in LMNB1 occupancy across *FXN*.

CRISPRi induces transcriptional repression by sterically blocking RNA polymerase and interacting with KAP1 to recruit heterochromatin-related silencing factors.[40,41] To test whether *FXN* peripheral repositioning is a consequence of KAP1-mediated recruitment of silencing factors, we introduced a point mutation into the KRAB A-box (Y46A), shown to abrogate KRAB-KAP1 interaction, and measured *FXN* positioning relative to the lamina.[42,43] Similar to KRAB, KRAB-Y46A recruitment to *FXN* significantly reduced transcript levels, *FXN* repositioned closer to the nuclear periphery, and more frequently localized within the H3K9me2-marked peripheral chromatin layer compared with Scr-CRISPRi controls (Figures 2A and S2A–S2C). We next targeted dCas9-eGFP alone to *FXN* to sterically block RNA polymerase using either three *FXN*-specific gRNAs or no gRNAs (Figures S2D and S2E).[44,45] dCas9-eGFP-mediated repression of *FXN* transcription also resulted in locus repositioning closer to the periphery, with a greater percentage of alleles localizing within the depth of H3K9me2-marked chromatin compared with negative controls (Figures 2B and S2F). Locus heterochromatinization may also have contributed to the repositioning phenotype, and we therefore measured the compaction of *FXN* and the surrounding region using DNA-FISH oligo probes targeting a 750 kb region encompassing the *FXN* locus. There was no significant difference in probe volume between Scr-CRISPRi and *FXN*-CRISPRi, in contrast to a significant difference in volume when comparing size-matched LAD and nonLAD regions (Figures 2C and S2G). We also performed a higher-resolution interrogation of locus compaction by super-resolution OligoSTORM imaging using probes targeting the *FXN* gene only (43 kb), and we observed no change in the radius of gyration of *FXN* in *FXN*-CRISPRi cells compared with Scr-CRISPRi controls, in contrast to a LAD and nonLAD (Figures 2D and S2H). Finally, we introduced shRNA to reduce FXN protein to account for the possibility that repositioning resulted from FXN protein depletion or secondary changes in cell state (Figures S2I and S2J). In shRNA-treated cells, *FXN* positioning relative to the lamina mirrored the positioning observed in empty vector-treated control cells (Figure S2K). Thus, neither the recruitment of heterochromatin modifiers by KRAB nor the loss of FXN protein itself can account for the repositioning effect.

Our perturbations resulted in differing levels of transcriptional repression, which provided an opportunity to determine whether there is an association between the degree of transcriptional repression and the change in *FXN* positioning. We found a dose-dependent relationship between transcriptional repression and the change in the distance of *FXN* from the nuclear lamina (compared with individual controls, Figure 2E). Further supporting this observation, introduction of *FXN*-CRISPRi resulted in a gradual increase in *FXN* repression over time, accompanied by a similar shift in locus positioning, moving progressively closer to the lamina (12, 24, and 48 h compared with 96 h; Figures S2L–S2N). Collectively, these results support a central and necessary role for transcription in driving spatial positioning of *FXN* relative to the nuclear periphery.

LAD boundary spatial positioning and structural plasticity are controlled by transcription

To test whether transcription influences the positioning of LAD boundary genes beyond *FXN*, we first integrated publicly available human fibroblast expression datasets with LAD boundaries identified in NTC fibroblasts. 53% of all LAD boundaries are flanked by an expressed gene (n = 3,663, TPM $\geq$ 1, within 100 kb; Figure 3A). Reciprocally, thousands of expressed protein-coding genes are within 100 kb of a

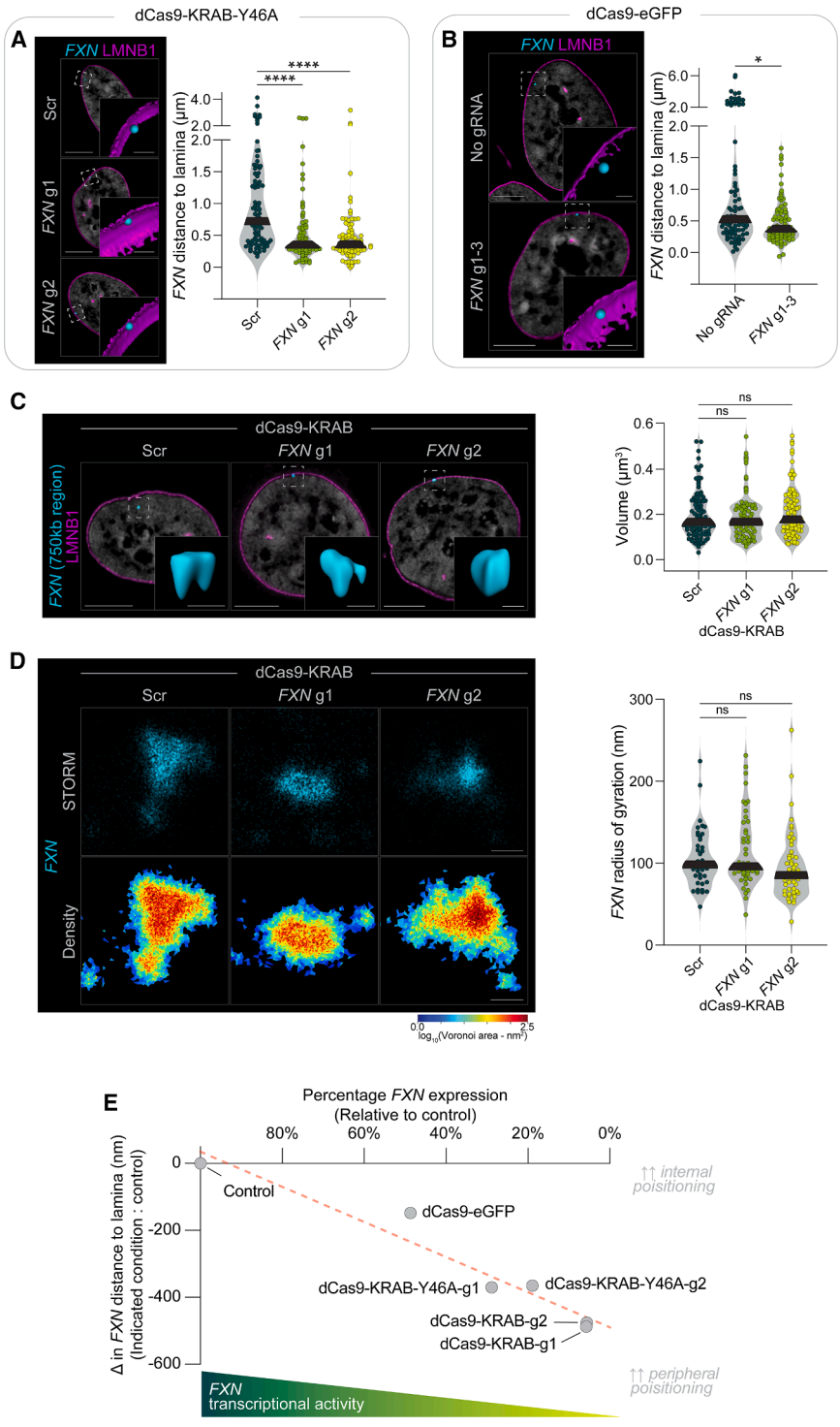


Figure 2. Transcriptional repression is sufficient to relocalize *FXN* to the nuclear lamina

(A) (Left) *FXN* immunoDNA-FISH with 3D reconstruction insets and (right) quantification of *FXN* positioning relative to the lamina in dCas9-KRAB-Y46A fibroblasts expressing indicated gRNAs. Kruskal-Wallis test.

(B) (Left) *FXN* immunoDNA-FISH with 3D reconstruction insets and (right) quantification of *FXN* positioning relative to the lamina in dCas9-EGFP fibroblasts expressing *FXN* gRNAs or no gRNAs. Kolmogorov-Smirnov test.

(C) (Left) Representative immunoDNA-FISH images using probes spanning a 750 kb region encompassing *FXN* with 3D reconstruction inset and (right) associated probe volume quantification in indicated conditions. Kruskal-Wallis test.

(D) (Left) Representative OligoSTORM images of *FXN* in indicated conditions (Gaussian rendering, top; heatmap rendering, bottom). (Right) Radius of gyration in indicated conditions. Kruskal-Wallis test.

(E) Correlation between the change in *FXN* expression versus the change in *FXN* positioning across represented conditions. For each condition, experimental values were compared with linked experimental controls. $R^2 = 0.94$.

Scale bars: 5 μm (A, B, and C), 1 μm (A, B, and C insets), and 100 nm (D). Black bars on violin plots, medians.

LAD boundary (Figure 3B). Gene ontology analysis showed expressed genes adjacent to LAD boundaries are linked to the development and morphogenesis of multiple organ systems (Table S1).[7–9] Informed by these findings, we assessed whether other LAD boundaries were governed by the transcription-positioning paradigm elucidated at the *FXN* locus (Figure 3C). We prioritized *ZNHIT6*, *HS1BP3*, and *C9orf72* as three additional LAD boundary genes that are broadly expressed across cell types, including NTC fibroblasts, and located within 100 kb of LMNB1-enriched chromatin ("LAD boundary"; Figures 3D, S3A, and S3B).[46] The distance of each locus from the nuclear periphery was not statistically different in NTC fibroblasts. Targeting dCas9-KRAB to the promoter of each LAD boundary gene resulted in targeted transcriptional repression, locus repositioning closer to the nuclear lamina, and more frequent association with H3K9me2-marked peripheral chromatin compared with NTC controls (Figures 3E, S3C, and S3D). To test the necessity of LAD boundary proximity, we targeted dCas9-KRAB to *GNB2* and *MRPL43*, two genes with similar expression patterns as the LAD boundary targets but located farther away from any LAD boundary ("LAD distal," 2.5 and 1.7 Mb away, respectively; Figures 3F, S3A, S3B, and S3E). In NTC fibroblasts, both loci are positioned away from the nuclear periphery and are only rarely localized within the depth of H3K9me2-marked peripheral chromatin (Figures 3G and

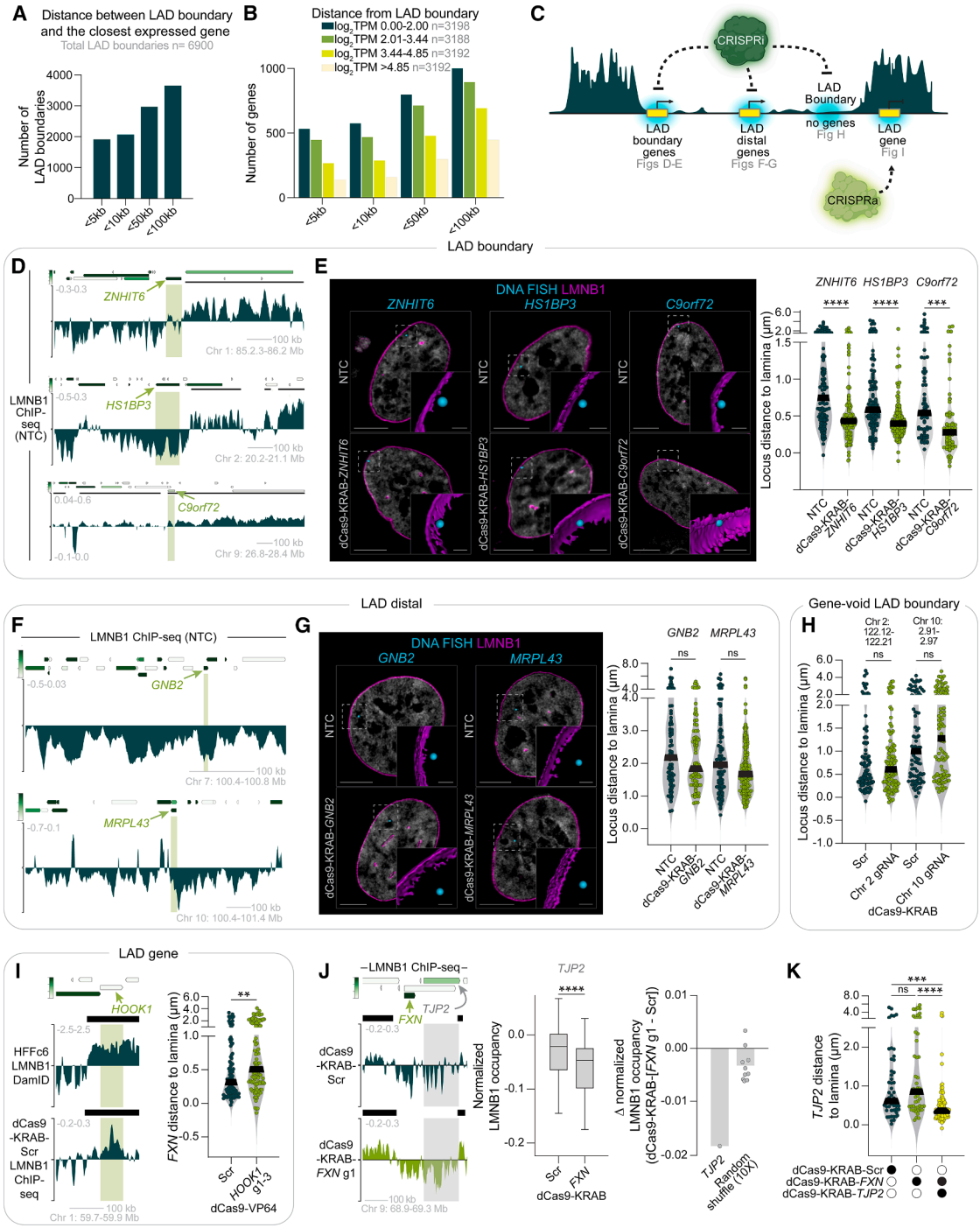


Figure 3. LAD boundary genes are sensitive to transcription-mediated changes in spatial positioning

(A) Number of LAD boundaries identified by LMNB1 ChIP-seq in NTC fibroblasts with expressed genes within specified distances from boundary (TPM > 1, HFFc6 RNA-seq: 4DNESFH3EHTU).

(B) Number of genes with indicated expression located within specified distances of a LAD boundary (NTC fibroblast LMNB1 ChIP-seq, HFFc6 RNA-seq).

(C) Schematic of CRISPRi- or CRISPRa-targeted regions relative to LADs and LAD boundaries, data in indicated panels.

(D) (Left) LMNB1 ChIP-seq tracks showing LAD boundary gene locations (highlighted) in NTC fibroblasts. Color bar is local gene expression (log_2TPM 0–3). Black bars indicate LADs.

(E) (Left) Representative immunoDNA-FISH and 3D reconstruction insets showing each LAD boundary gene and the nuclear lamina. (Right) Gene positioning relative to the lamina in NTC and locus-specific CRISPRi conditions. Kolmogorov-Smirnov test.

(F) (Left) LMNB1 ChIP-seq at LAD distal genes (highlighted). Color bar is local gene expression (log_2TPM 0–3). Black bars indicate LADs.

(legend continued on next page)

S3F). CRISPRi-mediated transcriptional repression of *GNB2* and *MRPL43* led to no change in the positioning of each locus relative to the lamina compared with NTC cells (Figures 3G, S3E, and S3F). To exclude the possibility that the positional changes are a consequence of dCas9-KRAB targeting independent of transcriptional repression, we targeted CRISPRi to two LAD boundaries devoid of annotated genes (Figures S3G and S3H). gRNAs targeting these regions were validated by confirming successful Cas9 recruitment and double-strand break formation, as assessed by Tracking of Indels by DEcomposition (TIDE) (Figure S3I).[47] Notably, CRISPRi targeting these two gene-void LAD boundaries did not alter their positioning compared with Scr-CRISPRi, indicating that LAD boundary gene repositioning is a consequence of transcriptional repression and not a secondary effect of dCas9-KRAB occupancy (Figure 3H). Together, these findings demonstrate that LAD boundary proximity confers susceptibility to transcriptional repression-mediated peripheral repositioning.

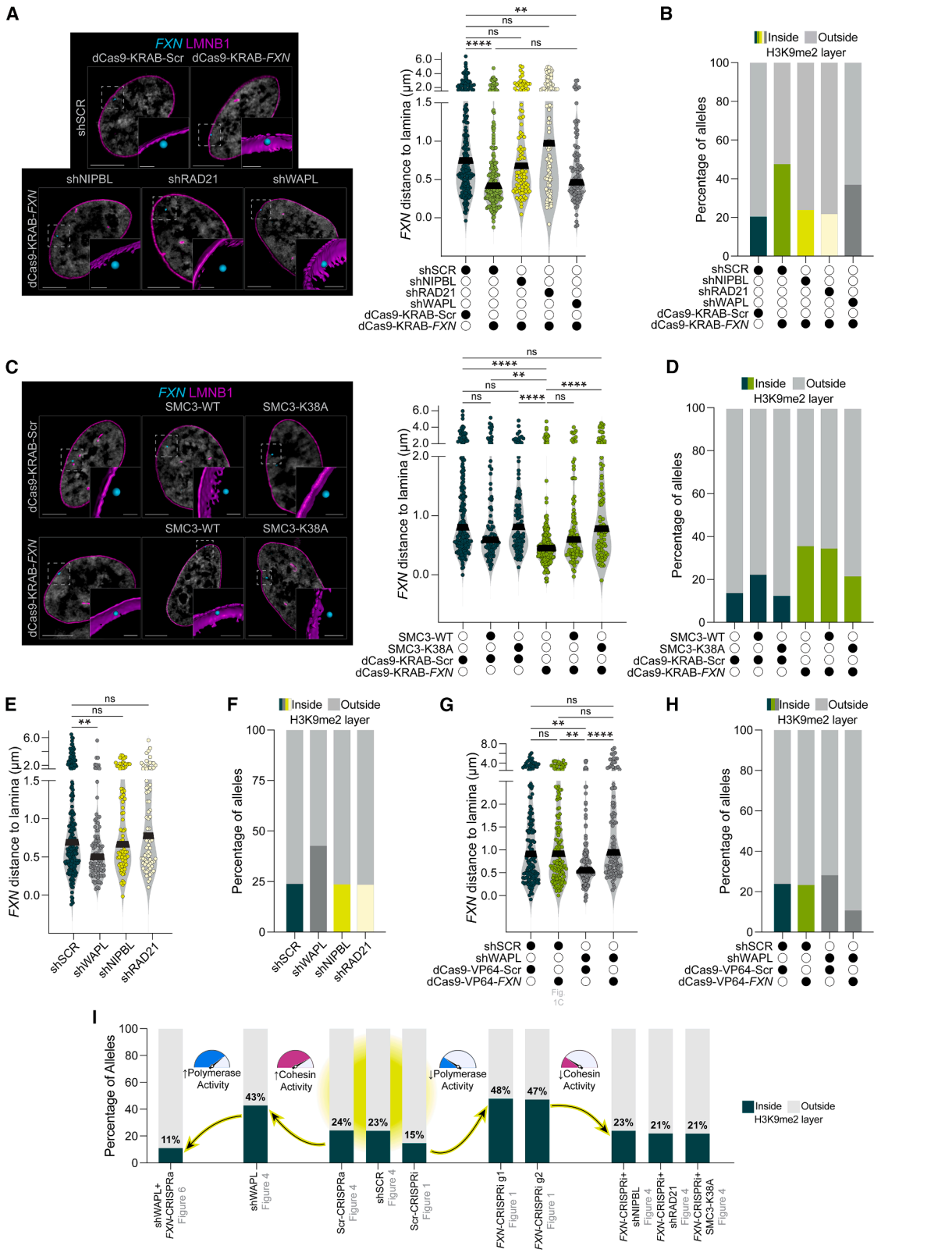
Given this finding, that LAD boundary-proximal gene transcription is necessary to maintain positioning away from the nuclear periphery, we sought to reciprocally test whether transcription is sufficient to reposition an internal LAD boundary gene from the nuclear periphery to the nuclear interior. CRISPRa-mediated forced transcriptional activation of *HOOK1*, a LAD gene approximately 50 kb internal to a LAD boundary, repositioned the locus away from the nuclear periphery, consistent with previous publications (Figures 3I, S3J, and S3K).[38,39,48–50]

Taken together, our data support a model in which transcription can drive the spatial positioning of LAD boundaries relative to the nuclear lamina and raises the possibility that transcription can also demarcate the location of new LAD boundaries along chromatin. To test this possibility, we mined our LMNB1 ChIP-seq data to examine the lamina-chromatin interaction changes effected by *FXN* transcriptional repression. Intriguingly, *FXN*-CRISPRi led to a spread of LMNB1 occupancy across *FXN* (Figure 1J), but we did not observe a corresponding increase in LMNB1 occupancy across the next actively transcribed gene, *TJP2* (Figure 3J). Consistent with this, *TJP2* remained positioned away from the periphery in both Scr- and *FXN*-CRISPRi conditions, mirroring the positioning of *FXN* in Scr-CRISPRi controls (Figure 3K). This suggests that the spread of LMNB1 into the adjacent nonLAD region following *FXN* transcriptional repression-mediated boundary disruption may be halted by the transcriptional activity of the next active gene, consistent with a recent study.[51] We therefore directly tested this possibility by simultaneously repressing *FXN* and *TJP2* with CRISPRi and found *TJP2* repositioned closer to the lamina, closely resembling the positioning of *FXN* upon transcriptional repression and the LAD upstream of *FXN* in controls (Figure 3K compared with Figures 1D and S3L–S3N). These findings demonstrate that active transcription proximal to a disrupted LAD boundary can demarcate the location of new boundaries and direct the positioning of genes in relation to the nuclear lamina, establishing a role for transcription in conferring LAD boundary structural and positional plasticity.

Dissecting the role of cohesin-transcription dynamics on *FXN* positioning

We next investigated the mechanisms by which transcriptional repression leads to changes in LAD boundary plasticity. Similar to LAD boundaries, TAD boundaries are dynamic, and their disruption by boundary bypass can result in local gene expression changes.[52–54] Cohesin activity regulates TAD boundary location, strength, and plasticity.[13,15,19,55] Comparison of TADs identified in human fibroblasts with NTC fibroblast LADs showed 1,859 shared TAD/LAD boundaries, consistent with previous reports (Figure S4A).[22,23,56] Of these shared boundaries, 64% feature at least one transcriptionally active gene within 100 kb, including *FXN* (n = 1,181, TPM > 1; Figure S4A). Genome-wide occupancy of the core cohesin subunit RAD21 demonstrated 81% of LAD/TAD boundaries overlap at least one RAD21 peak (n = 1,497; Figure S4A). RAD21 ChIP-seq showed RAD21 occupancy at the *FXN* promoter in Scr-CRISPRi, which was redistributed across the locus in *FXN*-CRISPRi (Figure S4B). Given the role of cohesin in regulating TAD boundary plasticity and the cohesin redistribution following transcriptional repression, we tested whether cohesin influences transcriptional repression-mediated *FXN* repositioning. *FXN*-CRISPRi was repeated with concurrent shRNA depletion of NIPBL, a factor that facilitates cohesin loading and translocation, or RAD21 (Figures S4C, S4D, S4F, and S4G).[17,57–59] Strikingly, depletion of either NIPBL or RAD21 prevented CRISPRi-mediated *FXN* peripheral repositioning and association with H3K9me2-marked chromatin, despite transcriptional repression (Figures 4A, 4B, S4G, and S4H). This effect was not limited to *FXN*; simultaneous CRISPRi and NIPBL depletion also prevented the repression-associated repositioning of *C9orf72*, another transcriptionally active LAD boundary gene with RAD21 occupancy (Figures S4I–S4L). Simultaneous depletion of WAPL, a factor that promotes cohesin unloading and whose loss leads to increased cohesin levels on chromatin and processivity,[15,19,60–62] did not lead to further *FXN* positioning closer to the lamina upon *FXN*-CRISPRi, likely because *FXN* was already peripherally positioned (Figures 4A, 4B, S4E, S4F, and S4H).

(G) (Left) ImmunoDNA-FISH and 3D reconstruction insets showing LAD distal genes and the lamina. (Right) Gene positioning relative to the lamina in NTC and locus-specific CRISPRi conditions. Mann-Whitney or Kolmogorov-Smirnov tests.
(H) Positioning of two LAD boundaries devoid of genes relative to the lamina in the indicated conditions. Mann-Whitney test.
(I) (Left) LMNB1 signal at *HOOK1*, an internal LAD boundary gene (highlighted) from HFFc6 LMNB1 DamID and Scr-CRISPRi LMNB1 ChIP-seq. Black bars indicate LADs. (Right) *HOOK1* positioning in indicated conditions. Kolmogorov-Smirnov test.
(J) (Left) LMNB1 ChIP-seq from Scr- and *FXN*-CRISPRi fibroblasts (*TJP2*, highlighted). Black bars indicate LADs. (Middle) Normalized *TJP2* LMNB1 occupancy in indicated conditions. Statistical comparisons across all 1 kb bins across the region indicated by the gray box were made using the paired Wilcoxon signed-rank test. Effect size (r) = 0.362 (moderate, Rosenthal's r method). (Right) Delta mean normalized LMNB1 signal between Scr- and *FXN*-CRISPRi at *TJP2* or 10,000 random regions matched for length and GC content (1,000 × 10). (K) *TJP2* positioning relative to the lamina in *FXN*-CRISPRi or *FXN*- and *TJP2*-CRISPRi. Kruskal-Wallis test. Scale bars: 5 and 1 μm (insets). Black bars on violin plots, medians.



(legend on next page)

Because cohesin-mediated alterations in TAD boundary structure reduce insulation and increase inter-TAD interactions,[52,63,64] we asked whether transcriptional repression-induced LAD boundary gene peripheral repositioning similarly alters interactions between adjacent LAD-nonLAD regions. Human fibroblast Micro-C datasets revealed two domains proximal to *FXN*: a 442 kb TAD overlapping the LAD upstream of *FXN* and a 185 kb TAD overlapping the nonLAD in which *FXN* resides (Figure S5A). To assess interaction changes across this interface, we performed DNA-FISH utilizing probes targeting *FXN* (cyan), the upstream LAD/TAD ("upstream LAD," yellow), and the nonLAD/TAD in which *FXN* resides ("downstream nonLAD," magenta; Figure S5A) and measured the inter-probe distances, a proxy for interaction frequency.[65] Consistent with Micro-C, *FXN* was closer to the downstream nonLAD than the upstream LAD in NTC fibroblasts (Figure S5B). CRISPRi-mediated transcriptional repression significantly reduced the distance between the upstream LAD and downstream nonLAD, indicating increased LAD-nonLAD interactions, and this was normalized by simultaneous NIPBL depletion (Figure S5C). Therefore, transcriptional repression disrupts LAD boundary positioning and local higher-order chromatin interactions in a cohesin-dependent manner.

We sought to understand how cohesin causes transcriptional repression-mediated LAD boundary repositioning. CTCF interacts with cohesin to limit its movement along DNA and is enriched at LAD and TAD boundaries.[9,11,66–71] CTCF depletion did not prevent CRISPRi-mediated *FXN* repositioning to the nuclear periphery (Figures S5D–S5F). CTCF depletion alone in NTC fibroblasts also resulted in no significant effect on *FXN* positioning relative to the lamina and minor changes in *FXN* expression (Figures S5G–S5I). H3K9me2 is enriched on lamina-associated chromatin, and H3K9me2 ChIP-seq in NTC fibroblasts confirmed enrichment across LADs (Figures S5J and S5K).[1,2,9,23,72] As with LMNB1, H3K9me2 enrichment modestly increased across *FXN* following CRISPRi compared with NTC controls (Figure S5K). However, simultaneous NIPBL depletion with *FXN*-CRISPRi showed sustained H3K9me2 enrichment across *FXN* versus random genomic regions and compared with NTC controls, despite *FXN* failing to reposition to the lamina (Figure S5K). Thus, transcriptional repression-induced changes in LAD boundary positioning cannot be clearly linked to CTCF or H3K9me2 enrichment.

Cohesin mediates genome folding via ATP-dependent loop extrusion, shown to be promoted by NIPBL.[17,18,20,73] Given our data that NIPBL depletion prevents CRISPRi-associated peripheral repositioning, we focused on the role of cohesin motor activity. Loop extrusion is driven by the ATPase activity of cohesin subunits SMC1 and SMC3 (structural maintenance of chromosomes).[74] Mutations in the Walker domain of SMC3 (K38A) permit cohesin loading onto chromatin but diminish ATP binding and hydrolysis, thereby attenuating loop extrusion activity.[74,75] Co-expression of SMC3-WT or SMC3-K38A in Scr-CRISPRi cells did not significantly alter *FXN* positioning, as assessed by distance to the lamina or by the fraction of alleles within the H3K9me2 layer, relative to Scr-CRISPRi. However, expression of SMC3-K38A, but not SMC-WT, in *FXN*-CRISPRi cells prevented *FXN* localization to the nuclear lamina and resulted in *FXN* distance to the lamina and percentage of alleles in peripheral heterochromatin similar to those observed in Scr-CRISPRi (Figures 4C, 4D, S5L, and S5M). These data demonstrate that cohesin-mediated loop extrusion is required for transcriptional repression-mediated LAD boundary repositioning.

These findings prompted us to more broadly investigate how cohesin activity and transcription are integrated to dictate LAD boundary gene positioning relative to the lamina under physiological conditions. To address this, we systematically modulated cohesin activity and transcription in NTC fibroblasts and assessed the effects on *FXN* positioning. NIPBL or RAD21 depletion had no significant effect on *FXN* positioning and produced only modest changes in expression compared with non-targeting scramble shRNA controls (shSCR; Figures 4E, 4F, S6A, and S6B). These results further demonstrated that CRISPRi-mediated repositioning cannot be attributed to cohesin displacement by CRISPRi or reduced cohesin activity. In contrast, WAPL depletion was sufficient to drive *FXN* to the nuclear periphery and significantly reduce *FXN* expression compared with shSCR controls (Figures 4E, 4F, S6A, and S6B). Importantly, there was no change in *WAPL* expression upon *FXN*-CRISPRi (Figure S6C). We next asked whether forced transcriptional activation could counteract this cohesin-mediated repositioning. As expected, WAPL depletion combined with non-targeting CRISPRa gRNAs resulted in *FXN* repression and peripheral localization. Strikingly, in cells expressing *FXN*-CRISPRa and shWAPL, *FXN* positioning was maintained away from the lamina despite elevated cohesin activity, demonstrating that forced transcriptional activity counteracts overactive cohesin-mediated peripheral repositioning (Figures 4G, 4H, S6D, and S6E). Together, our data support a model in which cohesin and transcription function as tunable molecular rheostats that jointly set the steady-state position of *FXN*

Figure 4. Cohesin and transcriptional activity drive *FXN* positioning

(A) (Left) *FXN* immunoDNA-FISH and 3D reconstruction insets and (right) *FXN* positioning relative to the nuclear lamina in *FXN*-CRISPRi with simultaneous shNIPBL, shRAD21, or shWAPL. Kruskal-Wallis test.

(B) Percentage of *FXN* alleles within peripheral H3K9me2 chromatin.

(C) (Left) *FXN* immunoDNA-FISH and 3D reconstruction insets. (right) *FXN* positioning relative to the lamina following introduction of SMC3 or SMC3-K38A, with or without *FXN*-CRISPRi. Kruskal-Wallis test.

(D) Percentage of *FXN* alleles within peripheral chromatin in indicated conditions.

(E) *FXN* positioning relative to the nuclear lamina in indicated shRNA-treated fibroblasts. Kruskal-Wallis test.

(F) Percentage of *FXN* alleles within peripheral H3K9me2 chromatin in indicated conditions.

(G) *FXN* positioning relative to the lamina upon *FXN*-CRISPRa with shSCR or shWAPL Kruskal-Wallis test.

(H) Percentage of *FXN* alleles within peripheral H3K9me2 chromatin.

(I) Cohesin and transcription are tunable molecular rheostats; adjusting the activity of either defines the positioning of *FXN* relative to nuclear lamina. Scale bars: 5 μm, 1 μm (insets). Black bars on violin plots, median distances.

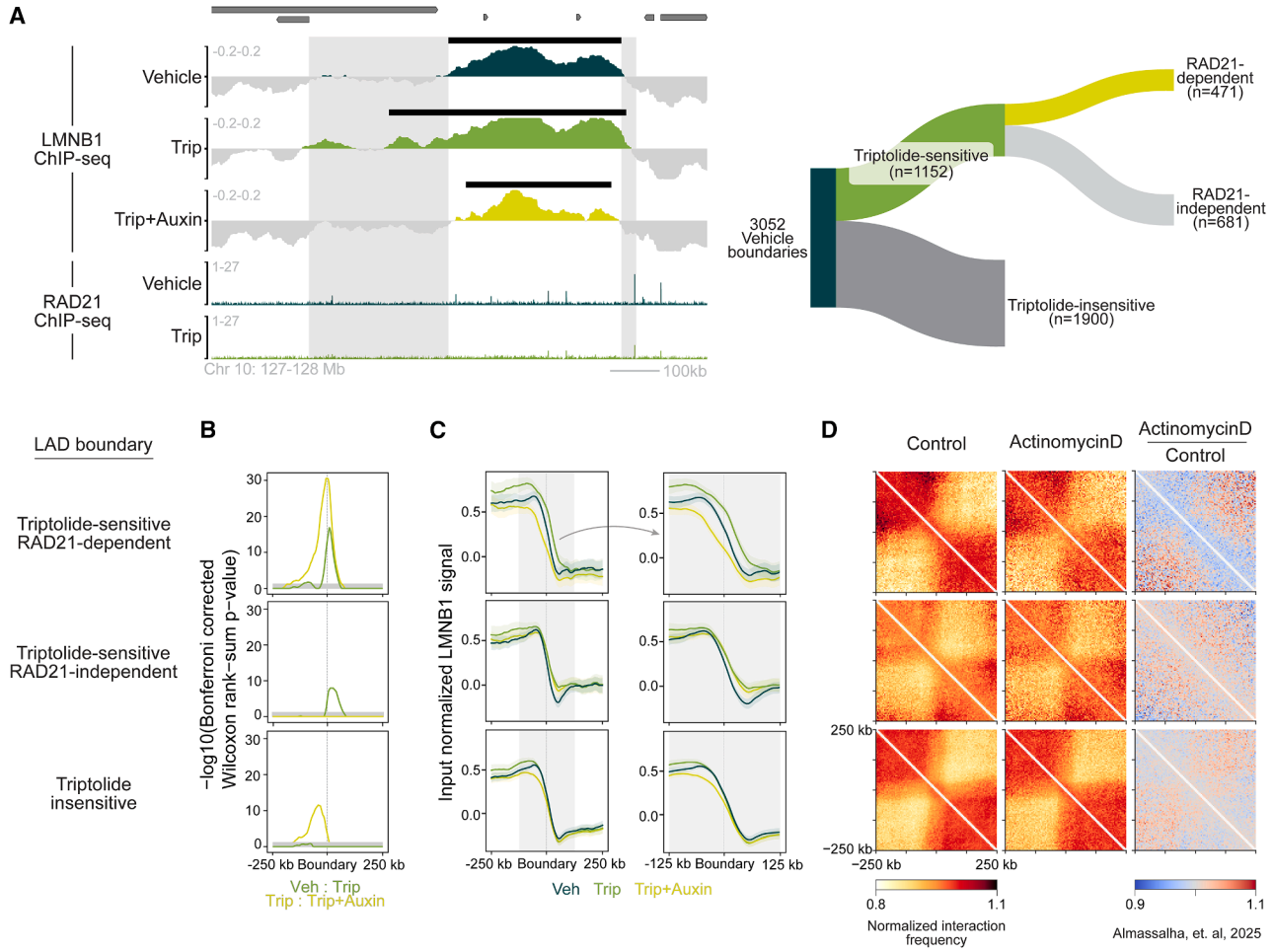


Figure 5. RAD21 loss rescues transcriptional repression-mediated changes at a subset of LAD boundaries

(A) (Top) Input-normalized, $\log_2$-transformed, LMNB1 ChIP-seq tracks at representative triptolide-sensitive, RAD21-dependent boundaries (highlighted). HCT116-mAID-RAD21 cells were treated with vehicle (DMSO), triptolide (200 nM, 12 h), or triptolide and an auxin analog (1 μM, 13 h). Black bars indicate LADs. Local genes are indicated as bars at the top. (Right) Sankey plot stratifying triptolide-sensitive boundaries, and of those, which are RAD21-dependent or -independent. (B–D) Analyses of indicated LAD boundary subtypes.

(B) Statistical analysis between indicated conditions (vehicle: triptolide or triptolide:triptolide+auxin) at LAD boundaries from three indicated categories (*x* axis: distance relative to boundary; *y* axis: corrected *p* value). Gray box indicates $p > 0.05$.

(C) LMNB1 occupancy at indicated boundary types, Right LAD boundary is shown.

(D) Aggregate contact maps from control and actinomycin D-treated cells at the indicated LAD boundary subtypes. Hi-C data, from Almassalha et al.[79]

relative to the lamina. Loss of transcriptional activity or overactivation of cohesin (via WAPL depletion) is sufficient to drive the *FXN* locus to the nuclear periphery. Reciprocal tuning of the opposing process rescues *FXN* spatial positioning in either case (Figure 4I).

Genome-wide analysis reveals cohesin- and transcription-dependent LAD boundary plasticity

To better appreciate the full scope of the transcription-cohesin interplay governing LAD boundary plasticity, we turned to a genome-wide approach. We performed LMNB1 ChIP-seq in RAD21-mAID-HCT116 cells to map LADs in the presence of the transcriptional inhibitor triptolide or DMSO (vehicle) and in the absence of RAD21. In these cells, the carboxy-terminus of endogenous RAD21 is fused to a mini auxin-inducible degron tag, allowing rapid and near-complete RAD21-specific degradation (Figure S6F).[76] Triptolide administration (12 h, 200 nM) significantly abrogates global transcriptional activity, consistent with previous reports (Figure S6G).[77] LADs identified by LMNB1 ChIP-seq in vehicle-treated cells largely overlapped with LADs from publicly available LMNB1 DamID in HCT116 cells (Figures S6H and S6I). Intriguingly, we noted examples of the spread of LMNB1 into the adjacent nonLAD following triptolide, similar to our observations at *FXN* (Figures 1J, 5A, and S6J). Of the 3052 LAD boundaries identified in the vehicle, 38% demonstrated a significant spread of LMNB1 occupancy into the adjacent nonLAD in triptolide-treated cells (hereafter "triptolide-sensitive," n = 1,152; Figures 5A–5C and S6J; see STAR Methods). To determine the role of cohesin in the shifting of these sensitive boundaries, we mapped LADs following

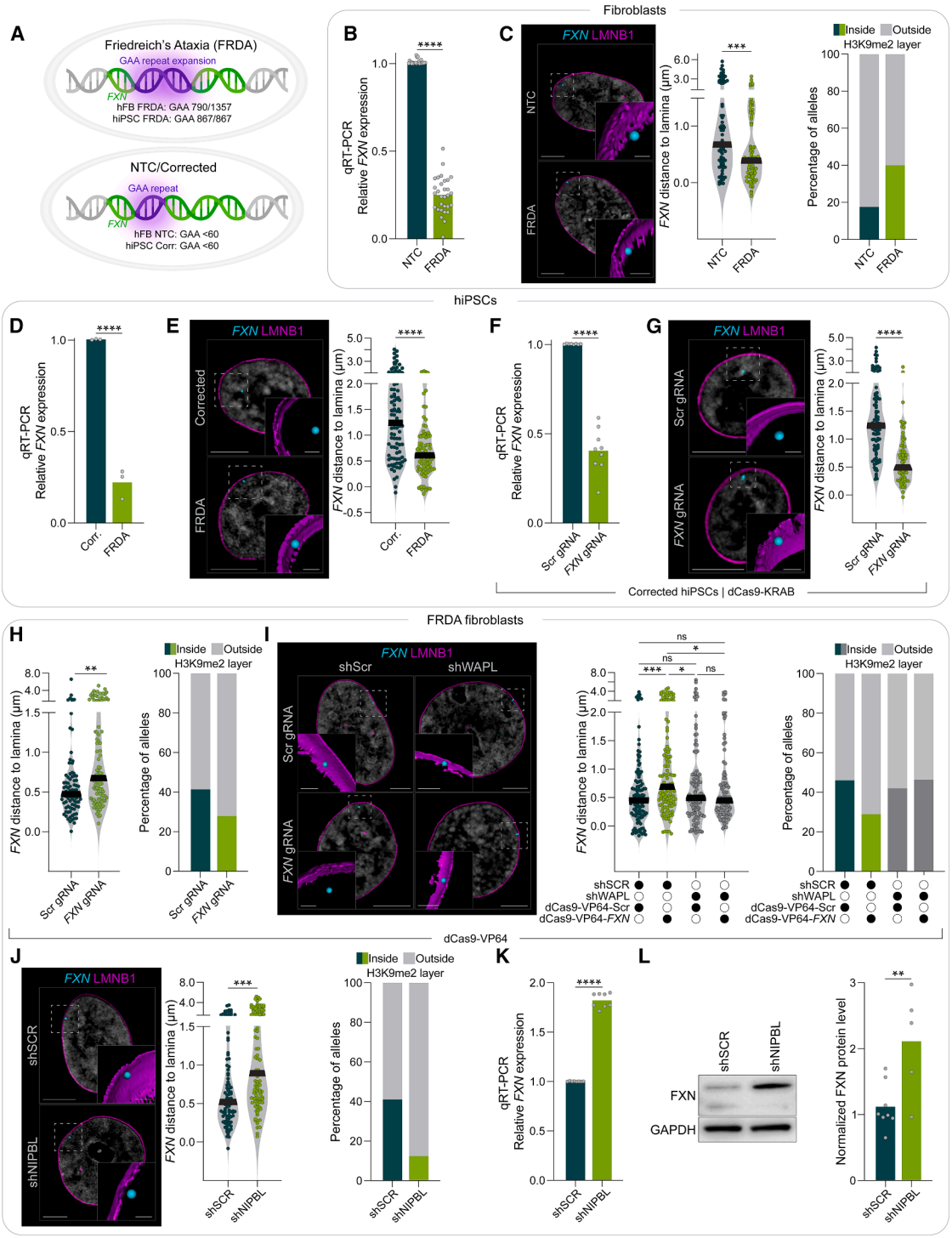


Figure 6. Transcriptionally repressed *FXN* in FRDA is positioned at the nuclear lamina by cohesin

(A) Schematic illustrating GAA nucleotide repeat within *FXN's* first intron in FRDA fibroblasts and hiPSCs (top) or NTC fibroblasts and isogenic corrected (Corr.) hiPSCs (bottom). The approximate reported number of GAA repeats associated with each cell type is indicated.

(B) *FXN* transcript levels in NTC and FRDA fibroblasts, normalized to levels in NTC. Bars represent means. Kolmogorov-Smirnov test.

(C) (Left) *FXN* immunoDNA-FISH and 3D reconstruction insets and (middle) *FXN* positioning relative to the lamina in NTC and FRDA fibroblasts. Mann-Whitney test. (Right) Percentage of *FXN* alleles localized within the peripheral H3K9me2 layer (thickness quantified in Figure S6M).

(D) *FXN* transcript levels in Corr. and FRDA hiPSCs, normalized to Corr. hiPSCs. Bars represent means. Unpaired *t* test.

(legend continued on next page)

triptolide treatment with RAD21 degradation (1 μM auxin analog 5-phenyl-indole-3-acetic acid [5-Ph-IAA], 13 h; Figure S6F). Simultaneous RAD21 degradation significantly attenuated LMNB1 spreading in nearly 41% of triptolide-sensitive boundaries ("RAD21-dependent," n = 471; Figures 5A–5C). RAD21 ChIP-seq demonstrated differences in RAD21 occupancy between vehicle and triptolide conditions, consistent with our results comparing Scr- with *FXN*-CRISPRi (Figures S4B and S6K). In addition, the time scale of these experiments suggests that transcription-mediated LAD boundary shifts are unlikely to be meaningfully affected by the cell cycle, given the approximately 17-h doubling time of HCT116 cells.[78]

Based on these findings, we asked whether extension of triptolide-sensitive LAD boundaries also resulted in altered interactions between surrounding regions. We mined recently published Hi-C datasets from HCT116 cells in which transcription was inhibited (actinomycin D, 4 μM, 1 h) and found that transcriptional inhibition in these cells resulted in a greater loss of interaction across the triptolide-sensitive, RAD21-dependent boundaries relative to that observed at triptolide-sensitive, RAD21-independent and triptolide-insensitive boundaries (Figure 5D).[79] These genome-wide analyses demonstrate that the cohesin-transcription interplay governs the structural plasticity of hundreds of LAD boundaries.

Transcriptionally repressed *FXN* in FRDA is positioned at the nuclear lamina by cohesin

Finally, we extended our mechanistic findings to a physiologically relevant context. FRDA is associated with a biallelic GAA trinucleotide repeat hyperexpansion in the first intron of *FXN* (Figure 6A).[80] Hyperexpanded GAA repeats form DNA secondary structures and alter local histone modifications that disrupt RNA polymerase loading and processivity, leading to a pathogenic reduction of *FXN* transcription.[81–87] The resultant loss of FXN protein causes devastating cardiac and neurologic pathologies, and clinical severity is directly correlated with the degree of *FXN* transcriptional repression.[88–90] Therefore, strategies aimed at increasing *FXN* transcript levels offer promising but underdeveloped therapeutic approaches.[91–94] FRDA provided an opportunity to study the relationship between transcriptional repression and *FXN* positioning independent of CRISPRi. We procured human fibroblasts derived from an FRDA patient and confirmed reduced *FXN* transcript levels compared with NTC fibroblasts (790/1,357 and <60/<60 GAA repeats per allele, respectively; Figures 6A and 6B).[95] *FXN* repression in FRDA fibroblasts is approximately 25% of NTC controls, comparable with that measured following KRAB-Y46A targeting to *FXN* (Figure S2B). As expected, transcriptional repression in FRDA cells corresponds with decreased FXN protein (Figure S6L). Consistent with a previous study showing the peripheral localization of a repeat-expanded *FXN* locus on an artificial construct, pathogenic *FXN* repression in FRDA fibroblasts is associated with *FXN* positioning at the nuclear periphery and a greater association with peripheral H3K9me2-marked chromatin compared with NTCs (Figures 6C and S6M).[6] ChIP-seq revealed comparable genome-wide LMNB1 occupancy between NTC and FRDA fibroblasts; however, LMNB1 occupancy is significantly increased across *FXN* in FRDA compared with NTC cells, mirroring *FXN*-CRISPRi compared with Scr-CRISPRi (Figures S6N and S6O). We noted no significant difference in the positioning of other loci on different chromosomes between NTC and FRDA fibroblasts by DNA-FISH or in *FXN* compaction between conditions by OligoSTORM (Figures S6P and S6Q).

Mirroring our data in fibroblasts, *FXN* transcriptional repression in FRDA human induced pluripotent stem cells (hiPSCs) correlates with *FXN* positioning closer to the nuclear periphery and more frequent association with peripheral H3K9me2-marked chromatin compared with isogenic corrected hiPSCs (Figures 6D, 6E, and S7A–S7D).[96,97] Moreover, CRISPRi targeting to *FXN* in the corrected hiPSCs was sufficient to relocalize the corrected *FXN* allele to the nuclear periphery (Figures 6F, 6G, S7D, and S7E). Despite differences in the spatial positioning of all *FXN* alleles between FRDA and NTC or corrected cells (as determined by immunoDNA-FISH), immunoRNA-FISH revealed that actively transcribing alleles were consistently located farther from the nuclear lamina and not significantly different between FRDA and NTC cells (Figures S7F–S7H). These findings demonstrate that both biological and experimental transcriptional repression of the boundary gene *FXN* leads to locus peripheral repositioning. More broadly, these experiments indicate *FXN* transcriptional repression in multiple FRDA cell types drives improper *FXN* repositioning to the nuclear periphery.

Building upon our findings in NTC fibroblasts, where *FXN* positioning is dictated by the relative balance between cohesin and transcription, we asked whether the same interplay governs *FXN* positioning in FRDA. We first verified cohesin occupancy across the *FXN* locus in FRDA fibroblasts (Figure S7I). Forced transcription of a peripherally localized LAD gene (*HOOK1*)

(E) (Left) *FXN* immunoDNA-FISH and 3D reconstruction insets and (right) *FXN* positioning relative to the nuclear lamina in Corr. and FRDA hIPSCs. Kolmogorov-Smirnov test.
(F) *FXN* transcript levels in Scr- and *FXN*-CRISPRi in Corr. hiPSCs. Bars represent means. Unpaired *t* test, Welch correction.
(G) (Left) *FXN* immunoDNA-FISH and 3D reconstruction insets and (right) *FXN* positioning relative to the lamina in Corr. hiPSCs expressing Scr- or *FXN*-CRISPRi. Mann-Whitney test.
(H) *FXN* positioning relative to the nuclear lamina in scr- or *FXN*-CRISPRa and associated H3K9me2-based stratification. Kolmogorov-Smirnov test.
(I) (Left) *FXN* immunoDNA-FISH and 3D reconstruction insets and (middle) *FXN* positioning relative to the nuclear lamina upon *FXN*-CRISPRa with simultaneous shSCR or shWAPL. Kruskal-Wallis test. (Right) Percentage of *FXN* alleles within H3K9me2 heterochromatin.
(J) (Left) *FXN* immunoDNA-FISH and 3D reconstruction insets and (middle) *FXN* positioning relative to the nuclear lamina in FRDA fibroblasts treated with shNIPBL or shSCR. Kolmogorov-Smirnov test. (Right) Percentage of *FXN* alleles localized inside or outside the peripheral H3K9me2-marked chromatin (thickness quantified in Figure S6M).
(K) *FXN* transcription in FRDA fibroblasts following shNIPBL relative to shSCR (qRT-PCR). Bars represent means. Unpaired *t* test, Welch correction.
(L) Immunoblot showing FXN levels in shNIPBL and shSCR FRDA cells and GAPDH-normalized quantification. Bars represent means. Unpaired *t* test. Scale bars: 5 and 1 μm (insets). Black bars on violin plots, medians.

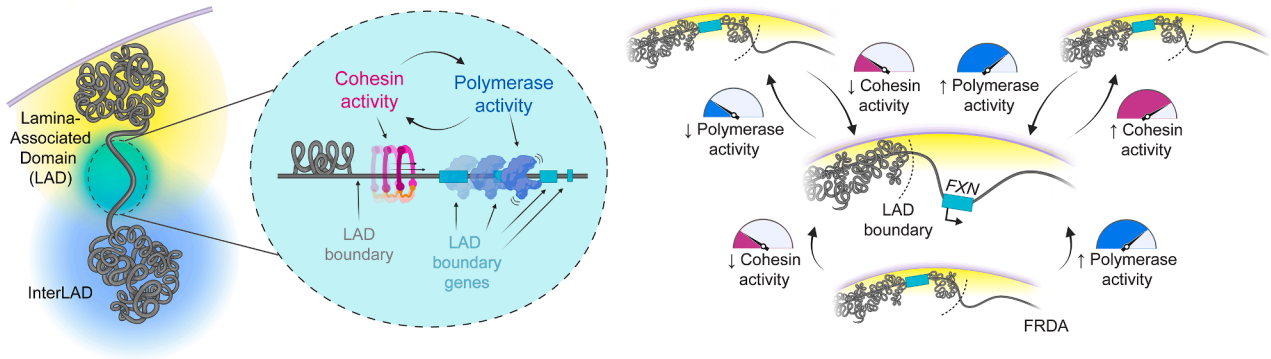


Figure 7. Transcription and cohesin tune LAD boundary gene positioning relative to the nuclear lamina

Transcription and cohesin activity act as molecular rheostats that tune LAD boundary gene structural plasticity and spatial positioning. Loss of transcriptional activity or increasing cohesin activity is sufficient to drive *FXN* to the nuclear periphery. Reciprocal tuning of the opposing process rescues *FXN* spatial positioning in either case. FRDA molecular pathology arises, in part, from an imbalance between the transcriptional activity and cohesin dynamics that govern LAD boundary gene positioning. Pathologic repression of *FXN* skews the system toward cohesin-directed positioning at the nuclear lamina, whereas retuning either transcription or cohesin activity is sufficient to restore positioning, with cohesin depletion additionally rescuing *FXN* expression.

was sufficient to drive its displacement from the lamina (Figure 3I). Similarly, CRISPRa-mediated transcriptional activation of *FXN* forced the locus away from the lamina in FRDA fibroblasts (Figures 6H, S7J, and S7K). Moreover, simultaneous enhancement of cohesin levels on chromatin via WAPL depletion blocked this transcriptional activation-driven movement, thus maintaining *FXN* at the lamina (Figures 6I and S7L–S7M). WAPL depletion had minimal effects on *FXN* positioning in FRDA fibroblasts compared with controls (Figure 6I).

Conversely, our findings demonstrating the necessity of cohesin in transcriptional repression-associated *FXN* peripheral positioning raise the possibility that cohesin may maintain peripherally localized *FXN* in FRDA and predict that reducing cohesin activity may partially normalize positioning (Figures 4A and 4B). We confirmed NIPBL depletion reduced chromatin-bound RAD21 in FRDA fibroblasts (Figures S7N–S7P). Strikingly, NIPBL depletion in FRDA fibroblasts led to *FXN* repositioning away from the nuclear periphery and less frequent association with H3K9me2-marked peripheral chromatin relative to shSCR controls (Figure 6J). Moreover, this repositioning of the pathogenic locus to the nuclear interior resulted in a nearly 2-fold statistically significant increase in *FXN* transcript and FXN protein levels compared with shSCR controls in FRDA cells (Figures 6K and 6L). NIPBL depletion in NTC fibroblasts did not affect *FXN* expression, indicating an FRDA-specific effect (Figures S7Q and S7R). Therefore, we reason that the release of *FXN* from the periphery in FRDA cells by NIPBL depletion most likely underlies the increase in its transcriptional activity. Furthermore, consistent with our previous results, we observed a maintenance of H3K9me2 enrichment across *FXN* following shNIPBL-mediated internal repositioning, suggesting local levels of H3K9me2 are unlinked to *FXN* positioning across the experimental conditions (Figure S7S). Collectively, our data demonstrate that FRDA molecular pathology arises, in part, from an imbalance between the transcriptional activity and cohesin dynamics that govern LAD boundary gene positioning. Pathologic repression of *FXN* skews the system toward cohesin-directed positioning at the nuclear lamina, whereas retuning either transcription or cohesin activity is sufficient to restore positioning, with cohesin depletion additionally rescuing *FXN* expression. These findings support a rheostat-like model in which dysregulated LAD boundary organization is both a driver of disease pathology and a tractable target for correction (Figure 7).

DISCUSSION

The 3D structure of the genome cannot simply be considered a static framework but rather is likely a dynamic and flexible entity, capable of varying across cell types and of adapting in response to stimuli. However, the mechanisms that endow the genome with plasticity remain elusive. Boundaries of genome organizational units have been implicated as important sites of genome variability and, accordingly, as critical areas of gene regulation. Here, using endogenous, locus-specific perturbations coupled with single-cell spatial measurements and genome-wide interrogations, we systematically modulate transcription and cohesin in multiple directions. We demonstrate that transcription and cohesin activity at LAD boundaries jointly act as tunable, rheostat-like determinants of LAD boundary integrity and spatial positioning. Moreover, we show that this mechanism is hijacked, but correctable, in human disease (Figure 7). In FRDA, re-tuning this balance can reposition the silenced locus to the nuclear interior and partially normalize *FXN* transcript and protein levels, the primary drivers of disease. Leveraging gain- and loss-of-function approaches and comprehensive locus-resolved dissections, our study merges previously segregated regulatory mechanisms, revealing that an established regulator of TAD organization and transcription intersects to instruct LAD boundary plasticity.

Several mechanisms may explain the functional antagonism we observed between transcription and cohesin. First, RNA polymerase and the related machinery may act as a physical barrier to cohesin. SMC proteins can bypass dCas9 and RNA polymerase in *in vitro* experiments[98,99]; however, the diverse compositions of megadalton transcriptional complexes may present a more substantial physical barrier *in vivo*. Second, nascent RNA—the product of transcription—may limit cohesin activity

or displace cohesin from chromatin. STAG proteins interact with RNA independently of cohesin, and cohesin can associate with splicing factors.[100,101] However, the biochemical basis for RNA serving as a barrier to cohesin translocation remains unclear. Third, both transcription and cohesin induce DNA supercoiling, and SMC activity is sensitive to DNA tension, raising the possibility for localized high levels of DNA torsion to act as a functional barrier by attenuating cohesin activity.[102,103] A similar mechanism was recently demonstrated, showing that CTCF insulator function depends on DNA tension *in vitro*.[99] Local variations in chromatin tension can also be influenced by the DNA sequence itself, as observed with nucleotide repeats such as those in FRDA.[104] Importantly, these mechanisms need not be mutually exclusive and may be interdependent.

Our findings demonstrate that forced transcriptional activation and NIPBL depletion are sufficient to reposition the endogenous, hyperexpanded *FXN* locus away from the nuclear lamina in FRDA fibroblasts. These results raise an important question regarding the temporal relationship between polymerase loading, transcriptional activation, and locus repositioning. One possibility is that *FXN* must disengage from the nuclear periphery prior to polymerase loading and transcriptional activation, consistent with the view of the nuclear periphery as an environment refractory to transcription.[105] Alternatively, polymerase loads onto peripherally sequestered chromatin, with transcription activation occurring subsequent to locus repositioning. A third possibility is that polymerase loading and transcription initiation can occur at the lamina itself in physiologic conditions, with locus movement occurring after transcription is established, challenging the prevailing paradigm that the nuclear lamina is intrinsically inhospitable to transcription. These further raise the question of whether transcriptional repression at the nuclear lamina is driven by spatial positioning or instead reflects a structural constraint imposed by genome folding. Our data suggest that cohesin may actively contribute to the transcriptionally repressive nature of LADs by stabilizing chromatin configurations unfavorable to polymerase loading and transcription. In this framework, repression would arise not from proximity to the lamina but from cohesin-dependent genome architecture at the periphery. Such a model is consistent with our data showing that reducing cohesin activity partially restores transcription and repositions *FXN* away from the lamina. Discriminating amongst these models will require direct, super-resolution dissection of polymerase dynamics, spatially resolved transcriptional bursting, and locus-specific positioning upon cohesin and transcription perturbations.

Our analyses reveal that over 15% of all LAD boundaries (471 of 3,052) are regulated by a transcription-cohesin paradigm, providing a foundation for identifying additional instances where changes in genome function can shape organizational boundaries. *FXN* pathogenic repression, which underlies the etiology of FRDA, provided an opportunity to investigate the interplay between transcription and LAD boundary positioning in disease, and several other genes related to nucleotide repeat disorders reside at organizational boundaries. In FRDA, the GAA expansion triggers multiple pathways that culminate in transcriptional repression.[6,86,106–109] Transcriptional repression promotes repositioning to the nuclear lamina, but restoring positioning of the endogenous, hyperexpanded locus also partially restores *FXN* expression. This suggests that peripheral positioning may reinforce long-term pathological silencing of the locus, particularly in post-mitotic cardiomyocytes and neurons.[110–113] New therapeutic strategies remain a focus for the FRDA community, with genome editing providing an exciting avenue for patients. Genome-editing machinery is less effective at penetrating heterochromatin.[114–117] Therefore, it will be exciting to explore whether repositioning the *FXN* locus to a more favorable environment in FRDA models enhances *FXN* expression or the efficacy of gene editing approaches. While we studied FRDA, several genes implicated in nucleotide repeat disorders have been shown to reside at organizational boundaries.[118]

Together, our findings suggest that genome function is not merely a consequence of nuclear architecture but an active, dynamic force that directs the structural plasticity of organizational boundaries. While this plasticity is essential for cellular diversity, its sensitivity to transcriptional changes also makes it vulnerable to disruption, providing a pathway for disease pathogenesis.

Limitations

Our conclusions regarding cohesin redistribution are based on RAD21 ChIP-seq, which provides ensemble occupancy and cannot resolve single-molecule kinetics. As a result, our data cannot distinguish between potential kinetic mechanisms, such as random versus specific movement, altered residence time, altered loading frequency, or pausing, that could underlie the changes in cohesin occupancy. Additionally, the loop-extrusion mutant experiments were performed expressing SMC3-K38A in the presence of endogenous SMC3. Although the loop extrusion mutant phenocopies cohesin loss-of-function, we cannot exclude partial complementation by endogenous complexes or dosage effects inherent to exogenous expression. Lastly, while we established mechanistic relationships in human fibroblast and iPSC models, it will be key to extend these findings to an *in vivo* FRDA model harboring the repeat expansion in the endogenous locus.

RESOURCE AVAILABILITY

Lead contact

Further information and requests for resources and reagents should be directed to and will be fulfilled by the lead contact, Rajan Jain (jainr@pennmedicine.upenn.edu).

Materials availability

All plasmids generated as part of this study are available by requesting the lead contact. Publicly available plasmids are noted in the STAR methods. All cell lines used in this study have been previously published.

Data and code availability

- All genomics data generated as part of this study have been deposited at GEO (GSE266505). Existing datasets used as part of this manuscript include: LMNB1 DamID: 4DNES24XA7U8 (HCT116) and 4DNESXZ4FW4T (HFFc6); HFFc6 RNA-seq: 4DNESFH3EHTU; Chromatin interaction in HFFc6: 4DNESWST3UBH (Micro-C) and 4DNESN49VY8X (Hi-C); Chromatin interaction in HCT116: GSE279166; and HFFc6 ATAC-seq: 4DNESMBA9T3L.

- All public datasets used in this study can be accessed through the 4DN Data Portal (https://data.4dnucleome.org) and the NCBI Gene Expression Omnibus (GEO; https://www.ncbi.nlm.nih.gov/geo/).
- This paper does not report original code.
- Any additional information required to reanalyze the data reported in this paper is available from the lead contact upon request.

ACKNOWLEDGMENTS

We thank the Jain laboratory, J. Phillips-Cremins, A. Raj, A. Martinez, M. Bartolomei, G. Blobel, J. Epstein, M. Lazar, N. Plachta, R. Bonasio, and C. Smith for helpful discussion and feedback. We thank Richard Abdill, Joshua Rhoades, and Yemin Lan for early bioinformatic help and Wenli Yang for early help with hiPSC culture. The work was funded by the National Institutes of Health (F31HL16011, T32GM008216, and T32HL007843 to A.K.; T32HD083185 to Z.G.; R21AG081795 to A.P.; R35HL166663 to R.J.; and U01DA052715 to M.L., E.F.J., and R.J.), the American Heart Association (24PRE1185932 to Z.G. and 26POST1561633 to K.K.H.), the Friedreich's Ataxia Research Alliance (to M.N. and R.B.W.), Burroughs Wellcome Foundation (to R.J.), and the W.W. Smith Charitable Trust (to R.J.). Some schematics were created using BioRender.com.

AUTHOR CONTRIBUTIONS

A.K. and R.J. conceived and designed the experiments. A.K., Q.W., Z.G., J.A.L., G.T.S., K.K.H., S.C.N., S.H., A.P., W.K., and P.P.S. generated reagents, performed imaging and molecular biology experiments, and analyzed data. A.K. and S.H. performed and analyzed the super-resolution microscopy. A.K., G.T.S., Q.W., J.A.L., B.S., N.D., and P.P.S. performed cell culture. A.K., R.L.-S., and P.P.S. performed and analyzed the genomics experiments. M.T.K., J.S.N., M.N., and R.B.W. generated and provided cell lines. M.L. and E.F.J. aided in the design and supervision of imaging experiments. M.L., E.F.J., and R.J. acquired funding for the project. A.K. and R.J. wrote the manuscript. R.J. supervised the project. All authors edited and approved the manuscript.

DECLARATION OF INTERESTS

The authors declare no competing interests.

STAR★METHODS

Detailed methods are provided in the online version of this paper and include the following:

- KEY RESOURCES TABLE
- EXPERIMENTAL MODEL AND STUDY PARTICIPANT DETAILS
  - Cell Culture
- METHOD DETAILS
  - Generation of RAD21-mAID cell line
  - Plasmids and lentiviral transduction
  - RNA isolation, preparation and qRT-PCR
  - Chromatin fractionation
  - Immunoblot analysis
  - Triptolide experiments
  - OligoFISH probe design and synthesis
  - ChIP and library preparation for sequencing
  - Immunofluorescence microscopy staining
  - DNA-FISH and DNA-FISH with immunofluorescence (DNA-FISH and immunoDNA-FISH)
  - RNA-FISH with immunofluorescence (immunoRNA-FISH)
  - Image acquisition
- QUANTIFICATION AND STATISTICAL ANALYSIS
  - Microscopy analysis
  - Genomic analyses
- QUANTIFICATION AND STATISTICAL ANALYSIS

SUPPLEMENTAL INFORMATION

Supplemental information can be found online at https://doi.org/10.1016/j.molcel.2026.04.019.

Received: June 10, 2024
Revised: December 24, 2025
Accepted: April 20, 2026
Published: May 12, 2026

REFERENCES

1. Peric-Hupkes, D., Meuleman, W., Pagie, L., Bruggeman, S.W.M., Solovei, I., Brugman, W., Gräf, S., Flicek, P., Kerkhoven, R.M., van Lohuizen, M., et al. (2010). Molecular maps of the reorganization of genome-nuclear lamina interactions during differentiation. Mol. Cell *38*, 603–613. https://doi.org/10.1016/j.molcel.2010.03.016.
2. Poleshko, A., Shah, P.P., Gupta, M., Babu, A., Morley, M.P., Manderfield, L.J., Ifkovits, J.L., Calderon, D., Aghajanian, H., Sierra-Pagán, J.E., et al. (2017). Genome-Nuclear Lamina Interactions Regulate Cardiac Stem Cell Lineage Restriction. Cell *171*, 573–587.e14. https://doi.org/10.1016/j.cell.2017.09.018.
3. Mattout, A., Pike, B.L., Towbin, B.D., Bank, E.M., Gonzalez-Sandoval, A., Stadler, M.B., Meister, P., Gruenbaum, Y., and Gasser, S.M. (2011). An EDMD mutation in C. elegans lamin blocks muscle-specific gene relocation and compromises muscle integrity. Curr. Biol. *21*, 1603–1614. https://doi.org/10.1016/j.cub.2011.08.030.
4. Shah, P.P., Lv, W., Rhoades, J.H., Poleshko, A., Abbey, D., Caporizzo, M.A., Linares-Saldana, R., Heffler, J.G., Sayed, N., Thomas, D., et al. (2021). Pathogenic LMNA variants disrupt cardiac lamina-chromatin interactions and de-repress alternative fate genes. Cell Stem Cell *28*, 938–954.e9. https://doi.org/10.1016/j.stem.2020.12.016.
5. Scaffidi, P., and Misteli, T. (2005). Reversal of the cellular phenotype in the premature aging disease Hutchinson-Gilford progeria syndrome. Nat. Med. *11*, 440–445. https://doi.org/10.1038/nm1204.
6. Silva, A.M., Brown, J.M., Buckle, V.J., Wade-Martins, R., and Lufino, M.M.P. (2015). Expanded GAA repeats impair FXN gene expression and reposition the FXN locus to the nuclear lamina in single cells. Hum. Mol. Genet. *24*, 3457–3471. https://doi.org/10.1093/hmg/ddv096.
7. Guelen, L., Pagie, L., Brasset, E., Meuleman, W., Faza, M.B., Talhout, W., Eussen, B.H., de Klein, A., Wessels, L., de Laat, W., et al. (2008). Domain organization of human chromosomes revealed by mapping of nuclear lamina interactions. Nature *453*, 948–951. https://doi.org/10.1038/nature06947.
8. Pal, M., Altamirano-Pacheco, L., Schauer, T., and Torres-Padilla, M.E. (2023). Reorganization of lamina-associated domains in early mouse embryos is regulated by RNA polymerase II activity. Genes Dev. *37*, 901–912. https://doi.org/10.1101/gad.350799.123.
9. Shah, P.P., Keough, K.C., Gjoni, K., Santini, G.T., Abdill, R.J., Wickramasinghe, N.M., Dundes, C.E., Karnay, A., Chen, A., Salomon, R.E.A., et al. (2023). An atlas of lamina-associated chromatin across twelve human cell types reveals an intermediate chromatin subtype. Genome Biol. *24*, 16. https://doi.org/10.1186/s13059-023-02849-5.
10. van Steensel, B., and Furlong, E.E.M. (2019). The role of transcription in shaping the spatial organization of the genome. Nat. Rev. Mol. Cell Biol. *20*, 327–337. https://doi.org/10.1038/s41580-019-0114-6.
11. Dixon, J.R., Selvaraj, S., Yue, F., Kim, A., Li, Y., Shen, Y., Hu, M., Liu, J.S., and Ren, B. (2012). Topological domains in mammalian genomes identified by analysis of chromatin interactions. Nature *485*, 376–380. https://doi.org/10.1038/nature11082.
12. Nora, E.P., Lajoie, B.R., Schulz, E.G., Giorgetti, L., Okamoto, I., Servant, N., Piolot, T., van Berkum, N.L., Meisig, J., Sedat, J., et al. (2012). Spatial partitioning of the regulatory landscape of the X-inactivation centre. Nature *485*, 381–385. https://doi.org/10.1038/nature11049.

13. Rao, S.S.P., Huang, S.C., Glenn St Hilaire, B., Engreitz, J.M., Perez, E.M., Kieffer-Kwon, K.R., Sanborn, A.L., Johnstone, S.E., Bascom, G.D., Bochkov, I.D., et al. (2017). Cohesin Loss Eliminates All Loop Domains. Cell *171*, 305–320.e24. https://doi.org/10.1016/j.cell.2017.09.026.

14. Thiecke, M.J., Wutz, G., Muhar, M., Tang, W., Bevan, S., Malysheva, V., Stocsits, R., Neumann, T., Zuber, J., Fraser, P., et al. (2020). Cohesin-Dependent and -Independent Mechanisms Mediate Chromosomal Contacts between Promoters and Enhancers. Cell Rep. *32*, 107929. https://doi.org/10.1016/j.celrep.2020.107929.

15. Wutz, G., Várnai, C., Nagasaka, K., Cisneros, D.A., Stocsits, R.R., Tang, W., Schoenfelder, S., Jessberger, G., Muhar, M., Hossain, M.J., et al. (2017). Topologically associating domains and chromatin loops depend on cohesin and are regulated by CTCF, WAPL, and PDS5 proteins. EMBO J. *36*, 3573–3599. https://doi.org/10.15252/embj.201798004.

16. Bauer, B.W., Davidson, I.F., Canena, D., Wutz, G., Tang, W., Litos, G., Horn, S., Hinterdorfer, P., and Peters, J.M. (2021). Cohesin mediates DNA loop extrusion by a "swing and clamp" mechanism. Cell *184*, 5448–5464.e22. https://doi.org/10.1016/j.cell.2021.09.016.

17. Davidson, I.F., Bauer, B., Goetz, D., Tang, W., Wutz, G., and Peters, J.M. (2019). DNA loop extrusion by human cohesin. Science *366*, 1338–1345. https://doi.org/10.1126/science.aaz3418.

18. Fudenberg, G., Imakaev, M., Lu, C., Goloborodko, A., Abdennur, N., and Mirny, L.A. (2016). Formation of Chromosomal Domains by Loop Extrusion. Cell Rep. *15*, 2038–2049. https://doi.org/10.1016/j.celrep.2016.04.085.

19. Gassler, J., Brandão, H.B., Imakaev, M., Flyamer, I.M., Ladstätter, S., Bickmore, W.A., Peters, J.M., Mirny, L.A., and Tachibana, K. (2017). A mechanism of cohesin-dependent loop extrusion organizes zygotic genome architecture. EMBO J. *36*, 3600–3618. https://doi.org/10.15252/embj.201798083.

20. Kim, Y., Shi, Z., Zhang, H., Finkelstein, I.J., and Yu, H. (2019). Human cohesin compacts DNA by loop extrusion. Science *366*, 1345–1349. https://doi.org/10.1126/science.aaz4475.

21. Vian, L., Pękowska, A., Rao, S.S.P., Kieffer-Kwon, K.R., Jung, S., Baranello, L., Huang, S.C., El Khattabi, L., Dose, M., Pruett, N., et al. (2018). The Energetics and Physiological Impact of Cohesin Extrusion. Cell *173*, 1165–1178.e20. https://doi.org/10.1016/j.cell.2018.03.072.

22. Fraser, J., Ferrai, C., Chiariello, A.M., Schueler, M., Rito, T., Laudanno, G., Barbieri, M., Moore, B.L., Kraemer, D.C.A., Aitken, S., et al. (2015). Hierarchical folding and reorganization of chromosomes are linked to transcriptional changes in cellular differentiation. Mol. Syst. Biol. *11*, 852. https://doi.org/10.15252/msb.20156492.

23. Kind, J., Pagie, L., de Vries, S.S., Nahidiazar, L., Dey, S.S., Bienko, M., Zhan, Y., Lajoie, B., de Graaf, C.A., Amendola, M., et al. (2015). Genome-wide maps of nuclear lamina interactions in single human cells. Cell *163*, 134–147. https://doi.org/10.1016/j.cell.2015.08.040.

24. Paulsen, J., Liyakat Ali, T.M., Nekrasov, M., Delbarre, E., Baudement, M.O., Kurscheid, S., Tremethick, D., and Collas, P. (2019). Long-range interactions between topologically associating domains shape the four-dimensional genome during differentiation. Nat. Genet. *51*, 835–843. https://doi.org/10.1038/s41588-019-0392-0.

25. Andrey, G., and Mundlos, S. (2017). The three-dimensional genome: regulating gene expression during pluripotency and development. Development *144*, 3646–3658. https://doi.org/10.1242/dev.148304.

26. Bonora, G., Plath, K., and Denholtz, M. (2014). A mechanistic link between gene regulation and genome architecture in mammalian development. Curr. Opin. Genet. Dev. *27*, 92–101. https://doi.org/10.1016/j.gde.2014.05.002.

27. Cremer, T., and Cremer, C. (2001). Chromosome territories, nuclear architecture and gene regulation in mammalian cells. Nat. Rev. Genet. *2*, 292–301. https://doi.org/10.1038/35066075.

28. Gilbert, N., Gilchrist, S., and Bickmore, W.A. (2005). Chromatin organization in the mammalian nucleus. Int. Rev. Cytol. *242*, 283–336. https://doi.org/10.1016/s0074-7696(04)42007-5.

29. He, M., Li, X., Xu, B., Lu, Y., Lai, J., Ling, Y., Liu, H., An, Z., Zhang, W., and Li, F. (2024). Reprogramming of 3D genome structure underlying HSPC development in zebrafish. Stem Cell Res. Ther. *15*, 172. https://doi.org/10.1186/s13287-024-03798-x.

30. Hnisz, D., Day, D.S., and Young, R.A. (2016). Insulated Neighborhoods: Structural and Functional Units of Mammalian Gene Control. Cell *167*, 1188–1200. https://doi.org/10.1016/j.cell.2016.10.024.

31. Hsia, C.R., Melters, D.P., and Dalal, Y. (2023). The Force is Strong with This Epigenome: Chromatin Structure and Mechanobiology. J. Mol. Biol. *435*, 168019. https://doi.org/10.1016/j.jmb.2023.168019.

32. Ma, Y., Kanakousaki, K., and Buttitta, L. (2015). How the cell cycle impacts chromatin architecture and influences cell fate. Front. Genet. *6*, 19. https://doi.org/10.3389/fgene.2015.00019.

33. Stadhouders, R., Vidal, E., Serra, F., Di Stefano, B., Le Dily, F., Quilez, J., Gomez, A., Collombet, S., Berenguer, C., Cuartero, Y., et al. (2018). Transcription factors orchestrate dynamic interplay between genome topology and gene regulation during cell reprogramming. Nat. Genet. *50*, 238–249. https://doi.org/10.1038/s41588-017-0030-7.

34. Kumar, P., Gholamalamdari, O., Zhang, Y., Zhang, L., Vertii, A., van Schaik, T., Peric-Hupkes, D., Sasaki, T., Gilbert, D.M., van Steensel, B., et al. (2023). Nucleolus and centromere TSA-Seq reveals variable localization of heterochromatin in different cell types. Preprint at bioRxiv. https://doi.org/10.1101/2023.10.29.564613.

35. van Schaik, T., Vos, M., Peric-Hupkes, D., Hn Celie, P., and van Steensel, B. (2020). Cell cycle dynamics of lamina-associated DNA. EMBO Rep. *21*, e50636. https://doi.org/10.15252/embr.202050636.

36. Gerber, J., Mühlenhoff, U., and Lill, R. (2003). An interaction between frataxin and Isu1/Nfs1 that is crucial for Fe/S cluster synthesis on Isu1. EMBO Rep. *4*, 906–911. https://doi.org/10.1038/sj.embor.embor918.

37. Gilbert, L.A., Larson, M.H., Morsut, L., Liu, Z., Brar, G.A., Torres, S.E., Stern-Ginossar, N., Brandman, O., Whitehead, E.H., Doudna, J.A., et al. (2013). CRISPR-mediated modular RNA-guided regulation of transcription in eukaryotes. Cell *154*, 442–451. https://doi.org/10.1016/j.cell.2013.06.044.

38. Perez-Pinera, P., Kocak, D.D., Vockley, C.M., Adler, A.F., Kabadi, A.M., Polstein, L.R., Thakore, P.I., Glass, K.A., Ousterout, D.G., Leong, K.W., et al. (2013). RNA-guided gene activation by CRISPR-Cas9-based transcription factors. Nat. Methods *10*, 973–976. https://doi.org/10.1038/nmeth.2600.

39. Kind, J., Pagie, L., Ortabozkoyun, H., Boyle, S., de Vries, S.S., Janssen, H., Amendola, M., Nolen, L.D., Bickmore, W.A., and van Steensel, B. (2013). Single-cell dynamics of genome-nuclear lamina interactions. Cell *153*, 178–192. https://doi.org/10.1016/j.cell.2013.02.028.

40. Peng, H., Gibson, L.C., Capili, A.D., Borden, K.L.B., Osborne, M.J., Harper, S.L., Speicher, D.W., Zhao, K., Marmorstein, R., Rock, T.A., et al. (2007). The structurally disordered KRAB repression domain is incorporated into a protease resistant core upon binding to KAP-1-RBCC domain. J. Mol. Biol. *370*, 269–289. https://doi.org/10.1016/j.jmb.2007.03.047.

41. Schultz, D.C., Ayyanathan, K., Negorev, D., Maul, G.G., and Rauscher, F.J., 3rd (2002). SETDB1: a novel KAP-1-associated histone H3, lysine 9-specific methyltransferase that contributes to HP1-mediated silencing of euchromatic genes by KRAB zinc-finger proteins. Genes Dev. *16*, 919–932. https://doi.org/10.1101/gad.973302.

42. Fujimori, T., Rios-Martinez, C., Thurm, A.R., Hinks, M.M., Doughty, B.R., Sinha, J., Le, D., Hafner, A., Greenleaf, W.J., Boettiger, A.N., et al. (2023). Single-cell chromatin state transitions during epigenetic memory formation. Preprint at bioRxiv. https://doi.org/10.1101/2023.10.03.560616.

43. Tycko, J., DelRosso, N., Hess, G.T., Aradhana, B., Banerjee, A., Mukund, A., Van, M.V., Ego, B.K., Yao, D., Spees, K., et al. (2020). High-Throughput

Discovery and Characterization of Human Transcriptional Effectors. Cell *183*, 2020–2035.e16. https://doi.org/10.1016/j.cell.2020.11.024.

44. Anderson, D.A., and Voigt, C.A. (2021). Competitive dCas9 binding as a mechanism for transcriptional control. Mol. Syst. Biol. *17*, e10512. https://doi.org/10.15252/msb.202110512.
45. Qi, L.S., Larson, M.H., Gilbert, L.A., Doudna, J.A., Weissman, J.S., Arkin, A.P., and Lim, W.A. (2013). Repurposing CRISPR as an RNA-guided platform for sequence-specific control of gene expression. Cell *152*, 1173–1183. https://doi.org/10.1016/j.cell.2013.02.022.
46. Uhlén, M., Fagerberg, L., Hallström, B.M., Lindskog, C., Oksvold, P., Mardinoglu, A., Sivertsson, Å., Kampf, C., Sjöstedt, E., Asplund, A., et al. (2015). Proteomics. Tissue-based map of the human proteome. Science *347*, 1260419. https://doi.org/10.1126/science.1260419.
47. Brinkman, E.K., Chen, T., Amendola, M., and van Steensel, B. (2014). Easy quantitative assessment of genome editing by sequence trace decomposition. Nucleic Acids Res. *42*, e168. https://doi.org/10.1093/nar/gku936.
48. Therizols, P., Illingworth, R.S., Courilleau, C., Boyle, S., Wood, A.J., and Bickmore, W.A. (2014). Chromatin decondensation is sufficient to alter nuclear organization in embryonic stem cells. Science *346*, 1238–1242. https://doi.org/10.1126/science.1259587.
49. Brueckner, L., Zhao, P.A., van Schaik, T., Leemans, C., Sima, J., Peric-Hupkes, D., Gilbert, D.M., and van Steensel, B. (2020). Local rewiring of genome-nuclear lamina interactions by transcription. EMBO J. *39*, e103159. https://doi.org/10.15252/embj.2019103159.
50. Tumbar, T., and Belmont, A.S. (2001). Interphase movements of a DNA chromosome region modulated by VP16 transcriptional activator. Nat. Cell Biol. *3*, 134–139. https://doi.org/10.1038/35055033.
51. Dauban, L., Eder, M., de Haas, M., Franceschini-Santos, V.H., Yañez-Cuna, J.O., Martinovic, M., van Schaik, T., Leemans, C., Teunissen, H., Rademaker, K., et al. (2025). Interactions between the genome and the nuclear lamina are multivalent and cooperative. Nat. Struct. Mol. Biol. *32*, 2335–2348. https://doi.org/10.1038/s41594-025-01655-w.
52. Lupiáñez, D.G., Kraft, K., Heinrich, V., Krawitz, P., Brancati, F., Klopocki, E., Horn, D., Kayserili, H., Opitz, J.M., Laxova, R., et al. (2015). Disruptions of topological chromatin domains cause pathogenic rewiring of gene-enhancer interactions. Cell *161*, 1012–1025. https://doi.org/10.1016/j.cell.2015.04.004.
53. Luppino, J.M., Park, D.S., Nguyen, S.C., Lan, Y., Xu, Z., Yunker, R., and Joyce, E.F. (2020). Cohesin promotes stochastic domain intermingling to ensure proper regulation of boundary-proximal genes. Nat. Genet. *52*, 840–848. https://doi.org/10.1038/s41588-020-0647-9.
54. Chakraborty, S., Kopitchinski, N., Zuo, Z., Eraso, A., Awasthi, P., Chari, R., Mitra, A., Tobias, I.C., Moorthy, S.D., Dale, R.K., et al. (2023). Enhancer-promoter interactions can bypass CTCF-mediated boundaries and contribute to phenotypic robustness. Nat. Genet. *55*, 280–290. https://doi.org/10.1038/s41588-022-01295-6.
55. Schwarzer, W., Abdennur, N., Goloborodko, A., Pekowska, A., Fudenberg, G., Loe-Mie, Y., Fonseca, N.A., Huber, W., Haering, C.H., Mirny, L., et al. (2017). Two independent modes of chromatin organization revealed by cohesin removal. Nature *551*, 51–56. https://doi.org/10.1038/nature24281.
56. Zheng, X., Hu, J., Yue, S., Kristiani, L., Kim, M., Sauria, M., Taylor, J., Kim, Y., and Zheng, Y. (2018). Lamins Organize the Global Three-Dimensional Genome from the Nuclear Periphery. Mol. Cell *71*, 802–815.e7. https://doi.org/10.1016/j.molcel.2018.05.017.
57. Ciosk, R., Shirayama, M., Shevchenko, A., Tanaka, T., Toth, A., Shevchenko, A., and Nasmyth, K. (2000). Cohesin's binding to chromosomes depends on a separate complex consisting of Scc2 and Scc4 proteins. Mol. Cell *5*, 243–254. https://doi.org/10.1016/s1097-2765(00)80420-7.
58. Kagey, M.H., Newman, J.J., Bilodeau, S., Zhan, Y., Orlando, D.A., van Berkum, N.L., Ebmeier, C.C., Goossens, J., Rahl, P.B., Levine, S.S., et al. (2010). Mediator and cohesin connect gene expression and chromatin architecture. Nature *467*, 430–435. https://doi.org/10.1038/nature09380.
59. Watrin, E., Schleiffer, A., Tanaka, K., Eisenhaber, F., Nasmyth, K., and Peters, J.M. (2006). Human Scc4 is required for cohesin binding to chromatin, sister-chromatid cohesion, and mitotic progression. Curr. Biol. *16*, 863–874. https://doi.org/10.1016/j.cub.2006.03.049.
60. Gandhi, R., Gillespie, P.J., and Hirano, T. (2006). Human Wapl is a cohesin-binding protein that promotes sister-chromatid resolution in mitotic prophase. Curr. Biol. *16*, 2406–2417. https://doi.org/10.1016/j.cub.2006.10.061.
61. Kueng, S., Hegemann, B., Peters, B.H., Lipp, J.J., Schleiffer, A., Mechtler, K., and Peters, J.M. (2006). Wapl controls the dynamic association of cohesin with chromatin. Cell *127*, 955–967. https://doi.org/10.1016/j.cell.2006.09.040.
62. Liu, N.Q., Maresca, M., van den Brand, T., Braccioli, L., Schijns, M.M.G.A., Teunissen, H., Bruneau, B.G., Nora, E.P., and de Wit, E. (2021). WAPL maintains a cohesin loading cycle to preserve cell-type-specific distal gene regulation. Nat. Genet. *53*, 100–109. https://doi.org/10.1038/s41588-020-00744-4.
63. Okhovat, M., VanCampen, J., Nevonen, K.A., Harshman, L., Li, W., Layman, C.E., Ward, S., Herrera, J., Wells, J., Sheng, R.R., et al. (2023). TAD evolutionary and functional characterization reveals diversity in mammalian TAD boundary properties and function. Nat. Commun. *14*, 8111. https://doi.org/10.1038/s41467-023-43841-8.
64. Hnisz, D., Weintraub, A.S., Day, D.S., Valton, A.L., Bak, R.O., Li, C.H., Goldmann, J., Lajoie, B.R., Fan, Z.P., Sigova, A.A., et al. (2016). Activation of proto-oncogenes by disruption of chromosome neighborhoods. Science *351*, 1454–1458. https://doi.org/10.1126/science.aad9024.
65. Linares-Saldana, R., Kim, W., Bolar, N.A., Zhang, H., Koch-Bojalad, B.A., Yoon, S., Shah, P.P., Karnay, A., Park, D.S., Luppino, J.M., et al. (2021). BRD4 orchestrates genome folding to promote neural crest differentiation. Nat. Genet. *53*, 1480–1492. https://doi.org/10.1038/s41588-021-00934-8.
66. Dowen, J.M., Fan, Z.P., Hnisz, D., Ren, G., Abraham, B.J., Zhang, L.N., Weintraub, A.S., Schujiers, J., Lee, T.I., Zhao, K., et al. (2014). Control of cell identity genes occurs in insulated neighborhoods in mammalian chromosomes. Cell *159*, 374–387. https://doi.org/10.1016/j.cell.2014.09.030.
67. Phillips-Cremins, J.E., Sauria, M.E., Sanyal, A., Gerasimova, T.I., Lajoie, B.R., Bell, J.S., Ong, C.T., Hookway, T.A., Guo, C., Sun, Y., et al. (2013). Architectural protein subclasses shape 3D organization of genomes during lineage commitment. Cell *153*, 1281–1295. https://doi.org/10.1016/j.cell.2013.04.053.
68. Rao, S.S.P., Huntley, M.H., Durand, N.C., Stamenova, E.K., Bochkov, I.D., Robinson, J.T., Sanborn, A.L., Machol, I., Omer, A.D., Lander, E.S., et al. (2014). A 3D map of the human genome at kilobase resolution reveals principles of chromatin looping. Cell *159*, 1665–1680. https://doi.org/10.1016/j.cell.2014.11.021.
69. Vietri Rudan, M., Barrington, C., Henderson, S., Ernst, C., Odom, D.T., Tanay, A., and Hadjur, S. (2015). Comparative Hi-C reveals that CTCF underlies evolution of chromosomal domain architecture. Cell Rep. *10*, 1297–1309. https://doi.org/10.1016/j.celrep.2015.02.004.
70. Nora, E.P., Goloborodko, A., Valton, A.L., Gibcus, J.H., Uebersohn, A., Abdennur, N., Dekker, J., Mirny, L.A., and Bruneau, B.G. (2017). Targeted Degradation of CTCF Decouples Local Insulation of Chromosome Domains from Genomic Compartmentalization. Cell *169*, 930–944.e22. https://doi.org/10.1016/j.cell.2017.05.004.
71. Busslinger, G.A., Stocsits, R.R., van der Lelij, P., Axelsson, E., Tedeschi, A., Galjart, N., and Peters, J.M. (2017). Cohesin is positioned in mammalian genomes by transcription, CTCF and Wapl. Nature *544*, 503–507. https://doi.org/10.1038/nature22063.

72. Poleshko, A., Smith, C.L., Nguyen, S.C., Sivaramakrishnan, P., Wong, K.G., Murray, J.I., Lakadamyali, M., Joyce, E.F., Jain, R., and Epstein, J.A. (2019). H3K9me2 orchestrates inheritance of spatial positioning of peripheral heterochromatin through mitosis. eLife *8*, e49278. https://doi.org/10.7554/eLife.49278.

73. Alonso-Gil, D., Cuadrado, A., Giménez-Llorente, D., Rodríguez-Corsino, M., and Losada, A. (2023). Different NIPBL requirements of cohesin-STAG1 and cohesin-STAG2. Nat. Commun. *14*, 1326. https://doi.org/10.1038/s41467-023-36900-7.

74. Ladurner, R., Bhaskara, V., Huis In 't Veld, P.J., Davidson, I.F., Kreidl, E., Petzold, G., and Peters, J.M. (2014). Cohesin's ATPase activity couples cohesin loading onto DNA with Smc3 acetylation. Curr. Biol. *24*, 2228–2237. https://doi.org/10.1016/j.cub.2014.08.011.

75. Hu, B., Itoh, T., Mishra, A., Katoh, Y., Chan, K.L., Upcher, W., Godlee, C., Roig, M.B., Shirahige, K., and Nasmyth, K. (2011). ATP hydrolysis is required for relocating cohesin from sites occupied by its Scc2/4 loading complex. Curr. Biol. *21*, 12–24. https://doi.org/10.1016/j.cub.2010.12.004.

76. Yesbolatova, A., Saito, Y., Kitamoto, N., Makino-Itou, H., Ajima, R., Nakano, R., Nakaoka, H., Fukui, K., Gamo, K., Tominari, Y., et al. (2020). The auxin-inducible degron 2 technology provides sharp degradation control in yeast, mammalian cells, and mice. Nat. Commun. *11*, 5701. https://doi.org/10.1038/s41467-020-19532-z.

77. Neguembor, M.V., Martin, L., Castells-García, Á., Gómez-García, P.A., Vicario, C., Carnevali, D., AlHaj Abed, J., Granados, A., Sebastian-Perez, R., Sottile, F., et al. (2021). Transcription-mediated supercoiling regulates genome folding and loop formation. Mol. Cell *81*, 3065–3081.e12. https://doi.org/10.1016/j.molcel.2021.06.009.

78. Ligasová, A., Strunin, D., Friedecký, D., Adam, T., and Koberna, K. (2015). A fatal combination: a thymidylate synthase inhibitor with DNA damaging activity. PLOS One *10*, e0117459. https://doi.org/10.1371/journal.pone.0117459.

79. Almassalha, L.M., Carignano, M., Liwag, E.P., Li, W.S., Gong, R., Acosta, N., Dunton, C.L., Gonzalez, P.C., Carter, L.M., Kakkaramadam, R., et al. (2025). Chromatin conformation, gene transcription, and nucleosome remodeling as an emergent system. Sci. Adv. *11*, eadq6652. https://doi.org/10.1126/sciadv.adq6652.

80. Campuzano, V., Montermini, L., Moltò, M.D., Pianese, L., Cossée, M., Cavalcanti, F., Monros, E., Rodius, F., Duclos, F., Monticelli, A., et al. (1996). Friedreich's ataxia: autosomal recessive disease caused by an intronic GAA triplet repeat expansion. Science *271*, 1423–1427. https://doi.org/10.1126/science.271.5254.1423.

81. Bidichandani, S.I., Ashizawa, T., and Patel, P.I. (1998). The GAA triplet-repeat expansion in Friedreich ataxia interferes with transcription and may be associated with an unusual DNA structure. Am. J. Hum. Genet. *62*, 111–121. https://doi.org/10.1086/301680.

82. Kim, E., Napierala, M., and Dent, S.Y.R. (2011). Hyperexpansion of GAA repeats affects post-initiation steps of FXN transcription in Friedreich's ataxia. Nucleic Acids Res. *39*, 8366–8377. https://doi.org/10.1093/nar/gkr542.

83. Ohshima, K., Montermini, L., Wells, R.D., and Pandolfo, M. (1998). Inhibitory effects of expanded GAA.TTC triplet repeats from intron I of the Friedreich ataxia gene on transcription and replication in vivo. J. Biol. Chem. *273*, 14588–14595. https://doi.org/10.1074/jbc.273.23.14588.

84. Punga, T., and Bühler, M. (2010). Long intronic GAA repeats causing Friedreich ataxia impede transcription elongation. EMBO Mol. Med. *2*, 120–129. https://doi.org/10.1002/emmm.201000064.

85. Sakamoto, N., Chastain, P.D., Parniewski, P., Ohshima, K., Pandolfo, M., Griffith, J.D., and Wells, R.D. (1999). Sticky DNA: self-association properties of long GAA.TTC repeats in R.R.Y triplex structures from Friedreich's ataxia. Mol. Cell *3*, 465–475. https://doi.org/10.1016/s1097-2765(00)80474-8.

86. Kumari, D., Biacsi, R.E., and Usdin, K. (2011). Repeat expansion affects both transcription initiation and elongation in friedreich ataxia cells. J. Biol. Chem. *286*, 4209–4215. https://doi.org/10.1074/jbc.M110.194035.

87. Matos-Rodrigues, G., van Wietmarschen, N., Wu, W., Tripathi, V., Koussa, N.C., Pavani, R., Nathan, W.J., Callen, E., Belinky, F., Mohammed, A., et al. (2022). S1-END-seq reveals DNA secondary structures in human cells. Mol. Cell *82*, 3538–3552.e5. https://doi.org/10.1016/j.molcel.2022.08.007.

88. Delatycki, M.B., and Corben, L.A. (2012). Clinical features of Friedreich ataxia. J. Child Neurol. *27*, 1133–1137. https://doi.org/10.1177/0883073812448230.

89. Hanson, E., Sheldon, M., Pacheco, B., Alkubeysi, M., and Raizada, V. (2019). Heart disease in Friedreich's ataxia. World J. Cardiol. *11*, 1–12. https://doi.org/10.4330/wjc.v11.i1.1.

90. Tsou, A.Y., Paulsen, E.K., Lagedrost, S.J., Perlman, S.L., Mathews, K.D., Wilmot, G.R., Ravina, B., Koeppen, A.H., and Lynch, D.R. (2011). Mortality in Friedreich ataxia. J. Neurol. Sci. *307*, 46–49. https://doi.org/10.1016/j.jns.2011.05.023.

91. Chutake, Y.K., Lam, C., Costello, W.N., Anderson, M., and Bidichandani, S.I. (2014). Epigenetic promoter silencing in Friedreich ataxia is dependent on repeat length. Ann. Neurol. *76*, 522–528. https://doi.org/10.1002/ana.24249.

92. Deutsch, E.C., Santani, A.B., Perlman, S.L., Farmer, J.M., Stolle, C.A., Marusich, M.F., and Lynch, D.R. (2010). A rapid, noninvasive immunoassay for frataxin: utility in assessment of Friedreich ataxia. Mol. Genet. Metab. *101*, 238–245. https://doi.org/10.1016/j.ymgme.2010.07.001.

93. Gottesfeld, J.M. (2019). Molecular Mechanisms and Therapeutics for the GAA·TTC Expansion Disease Friedreich Ataxia. Neurotherapeutics *16*, 1032–1049. https://doi.org/10.1007/s13311-019-00764-x.

94. Erwin, G.S., Grieshop, M.P., Ali, A., Qi, J., Lawlor, M., Kumar, D., Ahmad, I., McNally, A., Teider, N., Worringer, K., et al. (2017). Synthetic transcription elongation factors license transcription across repressive chromatin. Science *358*, 1617–1622. https://doi.org/10.1126/science.aan6414.

95. Cotticelli, M.G., Xia, S., Truitt, R., Doliba, N.M., Rozo, A.V., Tobias, J.W., Lee, T., Chen, J., Napierala, J.S., Napierala, M., et al. (2023). Acute frataxin knockdown in induced pluripotent stem cell-derived cardiomyocytes activates a type I interferon response. Dis. Model. Mech. *16*, dmm049497. https://doi.org/10.1242/dmm.049497.

96. Li, Y., Polak, U., Bhalla, A.D., Rozwadowska, N., Butler, J.S., Lynch, D.R., Dent, S.Y.R., and Napierala, M. (2015). Excision of Expanded GAA Repeats Alleviates the Molecular Phenotype of Friedreich's Ataxia. Mol. Ther. *23*, 1055–1065. https://doi.org/10.1038/mt.2015.41.

97. Li, Y., Li, J., Wang, J., Zhang, S., Giles, K., Prakash, T.P., Rigo, F., Napierala, J.S., and Napierala, M. (2022). Premature transcription termination at the expanded GAA repeats and aberrant alternative polyadenylation contributes to the Frataxin transcriptional deficit in Friedreich's ataxia. Hum. Mol. Genet. *31*, 3539–3557. https://doi.org/10.1093/hmg/ddac134.

98. Pradhan, B., Barth, R., Kim, E., Davidson, I.F., Bauer, B., van Laar, T., Yang, W., Ryu, J.K., van der Torre, J., Peters, J.M., et al. (2022). SMC complexes can traverse physical roadblocks bigger than their ring size. Cell Rep. *41*, 111491. https://doi.org/10.1016/j.celrep.2022.111491.

99. Davidson, I.F., Barth, R., Zaczek, M., van der Torre, J., Tang, W., Nagasaka, K., Janissen, R., Kerssemakers, J., Wutz, G., Dekker, C., et al. (2023). CTCF is a DNA-tension-dependent barrier to cohesin-mediated loop extrusion. Nature *616*, 822–827. https://doi.org/10.1038/s41586-023-05961-5.

100. Singh, A.K., Chen, Q., Nguyen, C., Meerzaman, D., and Singer, D.S. (2023). Cohesin regulates alternative splicing. Sci. Adv. *9*, eade3876. https://doi.org/10.1126/sciadv.ade3876.

101. Porter, H., Li, Y., Neguembor, M.V., Beltran, M., Varsally, W., Martin, L., Cornejo, M.T., Pezić, D., Bhamra, A., Surinova, S., et al. (2023). Cohesin-independent STAG proteins interact with RNA and R-loops and promote complex loading. eLife *12*, e79386. https://doi.org/10.7554/eLife.79386.

102. Gilbert, N., and Marenduzzo, D. (2025). Topological epigenetics: The biophysics of DNA supercoiling and its relation to transcription and genome instability. Curr. Opin. Cell Biol. *92*, 102448. https://doi.org/10.1016/j.ceb.2024.102448.

103. Ganji, M., Shaltiel, I.A., Bisht, S., Kim, E., Kalichava, A., Haering, C.H., and Dekker, C. (2018). Real-time imaging of DNA loop extrusion by condensin. Science *360*, 102–105. https://doi.org/10.1126/science.aar7831.

104. Majchrzak, M., Bowater, R.P., Staczek, P., and Parniewski, P. (2006). SOS repair and DNA supercoiling influence the genetic stability of DNA triplet repeats in Escherichia coli. J. Mol. Biol. *364*, 612–624. https://doi.org/10.1016/j.jmb.2006.08.093.

105. Shevelyov, Y.Y., and Nurminsky, D.I. (2012). The nuclear lamina as a gene-silencing hub. Curr. Issues Mol. Biol. *14*, 27–38.

106. Herman, D., Jenssen, K., Burnett, R., Soragni, E., Perlman, S.L., and Gottesfeld, J.M. (2006). Histone deacetylase inhibitors reverse gene silencing in Friedreich's ataxia. Nat. Chem. Biol. *2*, 551–558. https://doi.org/10.1038/nchembio815.

107. Greene, E., Mahishi, L., Entezam, A., Kumari, D., and Usdin, K. (2007). Repeat-induced epigenetic changes in intron 1 of the frataxin gene and its consequences in Friedreich ataxia. Nucleic Acids Res. *35*, 3383–3390. https://doi.org/10.1093/nar/gkm271.

108. Al-Mahdawi, S., Pinto, R.M., Ismail, O., Varshney, D., Lymperi, S., Sandi, C., Trabzuni, D., and Pook, M. (2008). The Friedreich ataxia GAA repeat expansion mutation induces comparable epigenetic changes in human and transgenic mouse brain and heart tissues. Hum. Mol. Genet. *17*, 735–746. https://doi.org/10.1093/hmg/ddm346.

109. Saveliev, A., Everett, C., Sharpe, T., Webster, Z., and Festenstein, R. (2003). DNA triplet repeats mediate heterochromatin-protein-1-sensitive variegated gene silencing. Nature *422*, 909–913. https://doi.org/10.1038/nature01596.

110. Gitler, A.D., and Tsuiji, H. (2016). There has been an awakening: Emerging mechanisms of C9orf72 mutations in FTD/ALS. Brain Res. *1647*, 19–29. https://doi.org/10.1016/j.brainres.2016.04.004.

111. Zhu, Q., Jiang, J., Gendron, T.F., McAlonis-Downes, M., Jiang, L., Taylor, A., Diaz Garcia, S., Ghosh Dastidar, S., Rodriguez, M.J., King, P., et al. (2020). Reduced C9ORF72 function exacerbates gain of toxicity from ALS/FTD-causing repeat expansion in C9orf72. Nat. Neurosci. *23*, 615–624. https://doi.org/10.1038/s41593-020-0619-5.

112. Schröder, C., Horsthemke, B., and Depienne, C. (2021). GC-rich repeat expansions: associated disorders and mechanisms. Med. Genet. *33*, 325–335. https://doi.org/10.1515/medgen-2021-2099.

113. Paulson, H. (2018). Repeat expansion diseases. Handb. Clin. Neurol. *147*, 105–123. https://doi.org/10.1016/b978-0-444-63233-3.00009-9.

114. Schep, R., Brinkman, E.K., Leemans, C., Vergara, X., van der Weide, R.H., Morris, B., van Schaik, T., Manzo, S.G., Peric-Hupkes, D., van den Berg, J., et al. (2021). Impact of chromatin context on Cas9-induced DNA double-strand break repair pathway balance. Mol. Cell *81*, 2216–2230.e10. https://doi.org/10.1016/j.molcel.2021.03.032.

115. Chen, E., Lin-Shiao, E., Trinidad, M., Saffari Doost, M., Colognori, D., and Doudna, J.A. (2022). Decorating chromatin for enhanced genome editing using CRISPR-Cas9. Proc. Natl. Acad. Sci. USA *119*, e2204259119. https://doi.org/10.1073/pnas.2204259119.

116. Sivakumar, A., and Cherqui, S. (2022). Advantages and Limitations of Gene Therapy and Gene Editing for Friedreich's Ataxia. Front. Genome Ed. *4*, 903139. https://doi.org/10.3389/fgeed.2022.903139.

117. Akdemir, K.C., Le, V.T., Kim, J.M., Killcoyne, S., King, D.A., Lin, Y.P., Tian, Y., Inoue, A., Amin, S.B., Robinson, F.S., et al. (2020). Somatic mutation distributions in cancer genomes vary with three-dimensional chromatin structure. Nat. Genet. *52*, 1178–1188. https://doi.org/10.1038/s41588-020-0708-0.

118. Sun, J.H., Zhou, L., Emerson, D.J., Phyo, S.A., Titus, K.R., Gong, W., Gilgenast, T.G., Beagan, J.A., Davidson, B.L., Tassone, F., et al. (2018). Disease-Associated Short Tandem Repeats Co-localize with Chromatin Domain Boundaries. Cell *175*, 224–238.e15. https://doi.org/10.1016/j.cell.2018.08.005.

119. Saito, Y., and Kanemaki, M.T. (2021). Targeted Protein Depletion Using the Auxin-Inducible Degron 2 (AID2) System. Curr. Protoc. *1*, e219. https://doi.org/10.1002/cpz1.219.

120. Horlbeck, M.A., Gilbert, L.A., Villalta, J.E., Adamson, B., Pak, R.A., Chen, Y., Fields, A.P., Park, C.Y., Corn, J.E., Kampmann, M., et al. (2016). Compact and highly active next-generation libraries for CRISPR-mediated gene repression and activation. eLife *5*, e19760. https://doi.org/10.7554/eLife.19760.

121. Beliveau, B.J., Kishi, J.Y., Nir, G., Sasaki, H.M., Saka, S.K., Nguyen, S.C., Wu, C.T., and Yin, P. (2018). OligoMiner provides a rapid, flexible environment for the design of genome-scale oligonucleotide in situ hybridization probes. Proc. Natl. Acad. Sci. USA *115*, E2183–E2192. https://doi.org/10.1073/pnas.1714530115.

122. Boettiger, A.N., Bintu, B., Moffitt, J.R., Wang, S., Beliveau, B.J., Fudenberg, G., Imakaev, M., Mirny, L.A., Wu, C.T., and Zhuang, X. (2016). Super-resolution imaging reveals distinct chromatin folding for different epigenetic states. Nature *529*, 418–422. https://doi.org/10.1038/nature16496.

123. Andrews, S. (2010). Babraham Bioinformatics – FastQC a quality control tool for high throughput sequence data. Babraham.ac.uk.

124. Chen, S., Zhou, Y., Chen, Y., and Gu, J. (2018). fastp: an ultra-fast all-in-one FASTQ preprocessor. Bioinformatics *34*, i884–i890. https://doi.org/10.1093/bioinformatics/bty560.

125. Langmead, B., and Salzberg, S.L. (2012). Fast gapped-read alignment with Bowtie 2. Nat. Methods *9*, 357–359. https://doi.org/10.1038/nmeth.1923.

126. Tarasov, A., Vilella, A.J., Cuppen, E., Nijman, I.J., and Prins, P. (2015). Sambamba: fast processing of NGS alignment formats. Bioinformatics *31*, 2032–2034. https://doi.org/10.1093/bioinformatics/btv098.

127. Danecek, P., Bonfield, J.K., Liddle, J., Marshall, J., Ohan, V., Pollard, M.O., Whitwham, A., Keane, T., McCarthy, S.A., Davies, R.M., et al. (2021). Twelve years of SAMtools and BCFtools. GigaScience *10*, giab008. https://doi.org/10.1093/gigascience/giab008.

128. Ramírez, F., Ryan, D.P., Grüning, B., Bhardwaj, V., Kilpert, F., Richter, A.S., Heyne, S., Dündar, F., and Manke, T. (2016). deepTools2: a next generation web server for deep-sequencing data analysis. Nucleic Acids Res. *44*, W160–W165. https://doi.org/10.1093/nar/gkw257.

129. Amemiya, H.M., Kundaje, A., and Boyle, A.P. (2019). The ENCODE Blacklist: Identification of Problematic Regions of the Genome. Sci. Rep. *9*, 9354. https://doi.org/10.1038/s41598-019-45839-z.

130. Lopez-deLisle, L., Rabbani, L., Wolff, J., Bhardwaj, V., Backofen, R., Grüning, B., Ramírez, F., and Manke, T. (2021). pyGenomeTracks: reproducible plots for multivariate genomic datasets. Bioinformatics *37*, 422–423. https://doi.org/10.1093/bioinformatics/btaa692.

131. Chen, Z., Djekidel, M.N., and Zhang, Y. (2021). Distinct dynamics and functions of H2AK119ub1 and H3K27me3 in mouse preimplantation embryos. Nat. Genet. *53*, 551–563. https://doi.org/10.1038/s41588-021-00821-2.

132. Quinlan, A.R., and Hall, I.M. (2010). BEDTools: a flexible suite of utilities for comparing genomic features. Bioinformatics *26*, 841–842. https://doi.org/10.1093/bioinformatics/btq033.

133. Neph, S., Kuehn, M.S., Reynolds, A.P., Haugen, E., Thurman, R.E., Johnson, A.K., Rynes, E., Maurano, M.T., Vierstra, J., Thomas, S., et al. (2012). BEDOPS: high-performance genomic feature operations. Bioinformatics *28*, 1919–1920. https://doi.org/10.1093/bioinformatics/bts277.

134. Larsson, J., Godfrey, A.J.R., and Gustafsson, P. algorithms, D.H.E., code, E.H., and Privé, F. (2024). Eulerr: Area-Proportional Euler and Venn Diagrams with Ellipses. R-Packages.

135. Khan, A., and Mathelier, A. (2017). Intervene: a tool for intersection and visualization of multiple gene or genomic region sets. BMC Bioinform. *18*, 287. https://doi.org/10.1186/s12859-017-1708-7.

136. Dekker, J., Belmont, A.S., Guttman, M., Leshyk, V.O., Lis, J.T., Lomvardas, S., Mirny, L.A., O'Shea, C.C., Park, P.J., Ren, B., et al. (2017). The 4D nucleome project. Nature *549*, 219–226. https://doi.org/10.1038/nature23884.

137. Reiff, S.B., Schroeder, A.J., Kırlı, K., Cosolo, A., Bakker, C., Mercado, L., Lee, S., Veit, A.D., Balashov, A.K., Vitzthum, C., et al. (2022). The 4D Nucleome Data Portal as a resource for searching and visualizing curated nucleomics data. Nat. Commun. *13*, 2365. https://doi.org/10.1038/s41467-022-29697-4.

138. Zhang, Y., Liu, T., Meyer, C.A., Eeckhoute, J., Johnson, D.S., Bernstein, B.E., Nusbaum, C., Myers, R.M., Brown, M., Li, W., et al. (2008). Model-based Analysis of ChIP-Seq (MACS). Genome Biol. *9*, R137. https://doi.org/10.1186/gb-2008-9-9-r137.

139. Team, R.C. (2021). R: A Language and Environment for Statistical Computing (R Foundation for Statistical Computing).

140. Wickham, H., Chang, W., Henry, L., Pedersen, T.L., Takahashi, K., Wilke, C., Woo, K., Yutani, H., Dunnington, D., Brand, T.v.D., et al. (2024) ggplot2: Create Elegant Data Visualisations Using the Grammar of Graphics. R-Packages.

141. Gu, Z. (2022). Complex heatmap visualization. Imeta *1*, e43. https://doi.org/10.1002/imt2.43.

142. Gu, Z., Eils, R., and Schlesner, M. (2016). Complex heatmaps reveal patterns and correlations in multidimensional genomic data. Bioinformatics *32*, 2847–2849. https://doi.org/10.1093/bioinformatics/btw313.

143. Krietenstein, N., Abraham, S., Venev, S.V., Abdennur, N., Gibcus, J., Hsieh, T.S., Parsi, K.M., Yang, L., Maehr, R., Mirny, L.A., et al. (2020). Ultrastructural Details of Mammalian Chromosome Architecture. Mol. Cell *78*, 554–565.e7. https://doi.org/10.1016/j.molcel.2020.03.003.

144. Akgol Oksuz, B., Yang, L., Abraham, S., Venev, S.V., Krietenstein, N., Parsi, K.M., Ozadam, H., Oomen, M.E., Nand, A., Mao, H., et al. (2021). Systematic evaluation of chromosome conformation capture assays. Nat. Methods *18*, 1046–1055. https://doi.org/10.1038/s41592-021-01248-7.

145. Flyamer, I.M., Illingworth, R.S., and Bickmore, W.A. (2020). Coolpup.py: versatile pile-up analysis of Hi-C data. Coolpup.py. Bioinformatics *36*, 2980–2985. https://doi.org/10.1093/bioinformatics/btaa073.

CellPress
OPEN ACCESS

STAR★METHODS

KEY RESOURCES TABLE

REAGENT or RESOURCE	SOURCE	IDENTIFIER
Antibodies		
Mouse monoclonal anti-Cas9 (*S.pyogenes*)	CST	Cat#14697;RRID: AB_2750916
Rabbit polyclonal anti-β-Actin	CST	Cat#4967;RRID: AB_330288
Rabbit monoclonal anti-GAPDH	CST	Cat#2118;RRID: AB_561053
Rabbit polyclonal anti-FXN	Abcam	Cat#ab175402;RRID: AB_2935904
Rabbit polyclonal anti-GFP	Abcam	Cat#ab290;RRID: AB_303395
Rabbit polyclonal anti-RAD21	Abcam	Cat#ab992;RRID: AB_2176601
Mouse monoclonal anti-RAD21	Millipore	Cat#05-908;RRID: AB_11214315
Rabbit polyclonal anti-Histone 3	Abcam	Cat#ab1791;RRID: AB_302613
Rabbit monoclonal anti-CTCF	CST	Cat#3418;RRID: AB_2086791
Rabbit monoclonal anti-SMC3	CST	Cat#5696;RRID: AB_10705575
Rabbit monoclonal anti-RBMX	CST	Cat#14794;RRID: AB_2798614
Mouse monoclonal anti-NIPBL	SCBT	Cat#sc374625;RRID: AB_10989775
Mouse monoclonal anti-WAPL	SCBT	Cat#sc365189;RRID: AB_10708870
Mouse monoclonal anti-hnRNPL	SCBT	Cat#sc32317;RRID: AB_627736
Rabbit polyclonal anti-LaminB1	Abcam	Cat#16048;RRID: AB_443298
Rabbit polyclonal anti-H3K9me2	Active Motif	Cat#39239;RRID: AB_2793199
Mouse monoclonal anti-OCT4	Millipore	Cat#MAB4419;RRID: AB_1977399
Mouse monoclonal anti-LaminAC	SCBT	Cat#sc376248;RRID: AB_10991536
Goat anti-Rabbit IgG (H+L) AF488	Thermo FIsher	Cat#A32731;RRID: AB_2633280
Goat anti-Mouse IgG (H+L) AF488	Thermo FIsher	Cat#A10680;RRID: AB_2534062
Goat anti-Rabbit IgG (H+L) AF555	Thermo FIsher	Cat#A32732;RRID: AB_2633281
Goat anti-Mouse IgG (H+L) AF555	Thermo FIsher	Cat#A32727;RRID: AB_2633276
Goat anti-Rabbit IgG (HRP-linked)	CST	Cat#7074;RRID: AB_2099233
Horse anti-Mouse IgG (HRP-linked)	CST	Cat#7076;RRID: AB_330924
Bacterial and virus strains		
NEB Stable Competent *E. coli* (High Efficiency)	NEB	Cat#C3040
Chemicals, peptides, and recombinant proteins		
Dulbecco's Modified Eagle Medium (DMEM)	Gibco	Cat#11965084
Fetal Bovine Serum	Cytiva	Cat#SH30910.03
Penicillin-Streptomycin	Thermo Fisher	Cat#15140122
Non-Essential Amino Acids	Thermo Fisher	Cat#11140050
TripLE Express	Gibco	Cat#12604021
Matrigel	Sigma	Cat#CLS356234
Essential 8 Medium	Thermo Fisher	Cat#A1517001
EDTA	Invitrogen	Cat#15575020
Thiazovinin	Cayman Chemical	Cat#14245-10
McCoy's 5A (Modified) Media	Gibco	Cat#166000082
5-Ph-IAA	MedChemExpress	Cat#HY-134653
Lipofectamine 2000	Invitrogen	Cat#11668019
PowerUp SYBR Green Master Mix	Thermo Fisher	Cat#A25742
DMSO	Sigma	Cat#D2650
Triptolide	CST	Cat#97539
Protein G Magnetic Beads	Invitrogen	Cat#10004D

(*Continued on next page*)

Continued

REAGENT or RESOURCE	SOURCE	IDENTIFIER
Bovine Serum Albumin	Sigma	Cat#A4503
DAPI	Sigma	Cat#D9542
SlowFade Antifade Mountant	Invitrogen	Cat#S36936
SSC	Invitrogen	Cat#15557036
Formamide	Thermo Fisher	Cat#BP227500
Dextran Sulfate	Thermo Fisher	Cat#BP1585
dNTPs	Invitrogen	Cat#18427088
RNase OUT	Invitrogen	Cat#1077019
TetraSpeck Fluorescent Beads	Invitrogen	Cat#T7279
Glucose Oxidase	Sigma	Cat#G2133
Catalase	Sigma	Cat#C3556
Q5 High-Fidelity Master Mix	NEB	Cat#0492
NEBuilder HiFi DNA Assembly Master Mix	NEB	Cat#2621
Critical commercial assays		
Expand High Fidelity PCR System	Roche	Cat#0473825001
QIAquick Gel Extraction Kit	Qiagen	Cat#28704
RNeasy Total RNA Extraction Kit	Qiagen	Cat#74106
iScript cDNA Synthesis Kit	BioRad	Cat#1708891
BCA Protein Assay Kit	Thermo Fisher	Cat#23225
NEBNext Ultra II DNA Library Prep Kit	NEB	Cat#E7770L
NEBNext Multiplex Oligos	NEB	Cat#E7630
NEBNext Library Quant Kit	NEB	Cat#E7630
Deposited data		
LMNB1/H3K9me2/RAD21 ChIP-seq in HCT116/human fibroblasts	This study	GEO: GSE266505
LMNB1 DamID in HCT116	https://data.4dnucleome.org/	4DNES24XA7U8
LMNB1 DamID in HFFc6	https://data.4dnucleome.org/	4DNESXZ4FW4T
RNA-seq in HFFc6	https://data.4dnucleome.org/	4DNESFH3EHTU
Micro-C data in HFFc6	https://data.4dnucleome.org/	4DNESWST3UBH
Hi-C data in HFFc6	https://data.4dnucleome.org/	4DNESN49VY8X
Chromatin Interaction data in HCT116	https://www.ncbi.nlm.nih.gov/geo	GEO: GSE279166
ATAC-seq in HFFc6	https://data.4dnucleome.org/	4DNESMBA9T3L
Experimental models: Cell lines		
Human NTC fibroblasts	Robert B. Wilson Lab	N/A
Human FRDA fibroblasts	Robert B. Wilson Lab	N/A
HCT116	ATCC	Cat#CCL-247;RRID: CVCL+0291
RAD21-mAID-HCT116	Masato Kanemaki Lab	N/A
LentiX-HEK293t	ATCC	Cat#CRL-1573;RRID: CVCL_0045
Human FRDA corrected iPSC	Marek Napierala Lab	N/A
Human FRDA iPSC	Marek Napierala Lab	N/A
Oligonucleotides		
shRNA oligonucleotides, see Data S1	This study	N/A
qRT-PCR primers, see Data S1	This study	N/A
gRNA sequences, see Data S1	This study	N/A
FISH probe sequences, see Data S1	This study	N/A
Recombinant DNA		
Lenti-(BB)-EF1a-KRAB-dCas9-P2A-BlastR	Addgene	Cat#118154
EF1a-NLS-dCas9-VP64-2A-Blast-WPRE	Addgene	Cat#61425

(*Continued on next page*)

Continued

REAGENT or RESOURCE	SOURCE	IDENTIFIER
pLV-U6-gRNA-UbC-eGFP-P2A-Bsr	Addgene	Cat#83925
pLenti-(BB)-EF1a-KRAB-Y46A-dCas9-P2A-BlastR	This study	N/A
pLenti-SpBsmBI-sgRNA-Hygro	Addgene	Cat#62205
pLenti-dCas9-EGFP-Blast	This study	N/A
pLJM1-Smc3	This study	N/A
pLJM1-Smc3_K38A	This study	N/A
SGEP-shFXN	This study	N/A
SGEP-shNTC	This study	N/A
pLKO.1-puro-shNIPBL	This study	N/A
pLKO.1-puro-shWAPL	This study	N/A
pLKO.1-puro-shCTCF	This study	N/A
pLKO.1-puro-RAD21	This study	N/A
psPAX2	Addgene	Cat#12260
pMD2.G	Addgene	Cat#12259
Software and algorithms		
Leica Lightning Process Deconvolution v3.5.6.21594	Leica	https://www.leica-microsystems.com/products/microscope-software/p/leica-las-x-ls/
NimOS NanoimagerTM Software v1.7.210222-3a3ef15d	ONI	https://oni.bio/nanoimager/
Imaris 8.1.2	Oxford Instruments	https://imaris.oxinst.com
MATLAB vR2020a	Mathworks	https://www.mathworks.com/products/matlab.html
Prism 10	GraphPad	https://www.graphpad.com
bcl2fastq2 v2.20	Illumina	https://support.illumina.com/sequencing/sequencing_software/bcl2fastq-conversion-software.html
Bowtie 2 v2.5.1	Langmead Lab / Johns Hopkins University	https://bowtie-bio.sourceforge.net/bowtie2/
fastp v0.23.2	OpenGene	https://github.com/OpenGene/fastp
sambamba v1.0.0	Sambamba project	https://github.com/biod/sambamba
deepTools v3.5.1	Max Planck Institute for Immunobiology and Epigenetics	https://deeptools.readthedocs.io/
MACS2 v2.2.6	MACS project	https://github.com/macs3-project/MACS
pyGenomeTracks v3.8	pyGenomeTracks project	https://pygenometracks.readthedocs.io/
FastQC v0.12.1	Babraham Bioinformatics	https://www.bioinformatics.babraham.ac.uk/projects/fastqc/
eulerr v7.0.2	CRAN / R Project	https://cran.r-project.org/package=eulerr
BEDTools v2.30.0	Quinlan Lab / University of Utah	https://bedtools.readthedocs.io/
BEDOPS v2.4.41	BEDOPS project	https://bedops.readthedocs.io/
samtools v1.16.1	SAMtools / HTSlib project	https://www.htslib.org/
Intervene v0.6.5	Intervene project	https://intervene.readthedocs.io/
R v4.3.2	R Project for Statistical Computing	https://www.r-project.org/
ggplot2 v3.4.4	tidyverse	https://ggplot2.tidyverse.org/
ComplexHeatmap v2.20.0	Bioconductor	https://bioconductor.org/packages/ComplexHeatmap/
MultiQC v1.33	Seqera	https://docs.seqera.io/multiqc/
featureCounts v2.1.1	Subread project	https://subread.sourceforge.net/featureCounts.html
DESeq2 v1.50.2	Bioconductor	https://bioconductor.org/packages/DESeq2/

(*Continued on next page*)

Continued

REAGENT or RESOURCE	SOURCE	IDENTIFIER
STAR v2.7.11b	STAR project	https://github.com/alexdobin/STAR
HISAT2 v2.2.0	Daehwan Kim Lab	https://daehwankimlab.github.io/hisat2/
Picard v3.4.0	Broad Institute	https://broadinstitute.github.io/picard/
Juicer v1.6	Aiden Lab	https://github.com/aidenlab/juicer
HiC-Pro v3.1.0	HiC-Pro project	https://github.com/nservant/HiC-Pro
cooler v0.10.4	Open2C	https://cooler.readthedocs.io/
cooltools v0.7.1	Open2C	https://cooltools.readthedocs.io/
bcl2fastq2 v2.20	Illumina	https://support.illumina.com/sequencing/sequencing_software/bcl2fastq-conversion-software.html

EXPERIMENTAL MODEL AND STUDY PARTICIPANT DETAILS

Cell Culture

Human skin NTC and FRDA immortalized fibroblast cells were kindly provided by Robert B. Wilson (Friedreich's Ataxia Center of Excellence at Penn. Medicine and Children's Hospital of Philadelphia) and cultured in DMEM (Gibco #11965084) supplemented with 10% fetal bovine serum (Cytiva SH30910.03), 1% penicillin/streptomycin (Invitrogen #15140122), and 1% non-essential amino acids (Invitrogen # 11140050) at 37°C with 20% O2 and 5% CO2. For virus production, LentiX-HEK293T cells (ATCC #CRL-1573) were cultured in DMEM supplemented with 10% fetal bovine serum and 1% penicillin/streptomycin at 37°C with 20% O2 and 5% CO2. For passaging, TrypLE Express Enzyme (Gibco #12604021) was used. Previously published hiPSCs were kindly provided by the Marek Napierala Laboratory (UT Southwestern Medical Center) and cultured in 6-well plates coated with Matrigel (Sigma #CLS356234) at 37°C with 20% O2 and 5% CO2 andmaintained in complete media comprised of Essential 8 medium with Essential 8 supplement added (Thermo Fisher #A1517001). hiPSCs were passaged every 3-5 days using 0.5mM EDTA (Invitrogen #15575020) and cultured in complete media with 3 μM Thiazovinvin (Cayman Chemical #14245-10) overnight before returning to complete media without Thiazovinvin. RAD21-mAID-HCT116 cells were kindly provided by the Masato Kanemaki Laboratory (National Institute of Genetics). RAD21-mAID-HCT116 and HCT116 (ATTC #CCL-247) cells were cultured in McCoy's (Invitrogen #16600082) supplemented with 10% fetal bovine serum, and 1% penicillin/streptomycin at 37°C with 20% O2 and 5% CO2.

METHOD DETAILS

Generation of RAD21-mAID cell line

RAD21-mAID-HCT116 cells were generated by insertion of the mAID-mClover epitope tag into the C-terminus of the endogenous RAD21 using CRISPR/Cas9 into an HCT116 cell line in which OsTIR1(F74G) was already inserted, as outlined as previously published.[119] The sequence gRNA used to target RAD21 was: CCAAGGTTCCATATTATATA. The gRNA was cloned into pX330-U6-Chimeric_BB-CBH-hSPCas9 (Addgene #42230) downstream of a U6 promoter using the BbsI site. The 5' and 3' homology arms were cloned into pMK278 (mClover-Hygro, Addgene #72794).

The 5′ homology arm (361 bp) was Ccccatccccaccccatgacacaaacacctcactaggctccatctctaacactgggaaattacgtttcagcatgagatttg-gaggggacaaatattcaaactgtatcagcatcctc
actgaattactactttattatacagattaagttacccttttttggttttatttcagCGTGCTCTTGCTAAAACTGGAGCTGAATCTATCAGTTTGCTTGAGTTATG
TCGAAATACGAACAGAAAACAAGCTGCCGCAAAGTTCTACAGCTTCTTGGTTCTTAAAAAGCAGCAAGCTATTGAGCTGACACAG
GAAGAACCGTACAGTGACATCATCGCAACACCTGGACCAAGGTTCCATATTATA

The 3′ homology arm (483 bp) was agctagaagcattatagctagtgtttgattcactagtgcttacaaattgcccccatgtgtaggggacacagaaccctttga-gaaaacttagatttttgtctgtacaaagtctttgccttttc
cttcttcatttttttccagtacattaaatttgtcaatttcatctttgagggaaactgattagatgggttgtgtttgtgttctgatggagaaaacagcaccccaaggactcagaagatgatttta
acagttcagaacagatgtgtgcaatattggtgcatgtaataatgttgagtggcagtcaaaagtcatgatttttatcttagttcttcattactgcattgaaaaggaaaacctgtctgaga aa
atgcctgacagtttaatttaaaactatggtgtaagtctttgacaagaaaaaaaaacaaacaaacacttctttccatcagtaacactggcaatcttcctgttaaccactctcctta

The 5′ arm was cloned immediately upstream of the mAID and the 3′ arm was cloned downstream of the HygoR cassette in pMK278. After sequence verifying the plasmids, OsTIR1(F74G)-HCT116 cells were targeted as described and single clones were isolated. The bi-allelic insertion was verified using PCR by the Kanemaki laboratory. All plasmids are available on Addgene or available by request to Dr. Kanemaki. RAD21 depletion was verified using immunoblotting as shown in the manuscript. 0.4 M cells/well were seeded on a 6-well tissue culture plate and grown on a standard cell culture condition. Once cells reached approximately 60% confluence, 1 μM 5-Ph-IAA was added and re-incubated for 12 hours. 5-Ph-IAA was provided by the Kanemaki laboratory and is now commercially available from MedChemExpress (HY-134653). After incubation, cells were then harvested by trypsinization and lysed

with lysis buffer containing 10 mM HEPES (pH 7.9), 3 mM $MgCl_2$, 5 mM KCl, 150 mM NaCl, 0.1 mM EDTA, 0.5% NP-40, and 250 units of Benzonase. Protein concentrations were determined using a bicinchoninic acid assay kit with bovine serum albumin as the standard. The protein concentrations were normalized, and 10 μg of samples were analyzed using immunoblotting.

Plasmids and lentiviral transduction

CRISPRi (dCas9-KRAB) expression constructs were generated as follows: Lenti-(BB)-EF1a-KRAB-dCas9-P2A-BlastR (Addgene #118154) was linearized using the BsmBI restriction enzyme (NEB #R0739) at standard conditions. Gene-specific oligos were selected from publicly available web resources (CHOPCHOP v3 chopchop.cbu.uib.no, Broad institute CRISpick portals.broadinstitute.org/gppx/crisprick/publick) or previously published datasets.[120] Phosphorylated and annealed oligos were ligated into the digested plasmid using T4 DNA ligase (Thermo Fisher #15224017). The introduction of each gRNA oligo was sequence verified by nanopore whole-plasmid sequencing (Plasmidsaurus). Per gene, gRNAs most successful at transcriptional repression were selected for individual introduction into human fibroblasts *via* lentiviral infection for 48 hours followed by 48 hours of selection by Blasticidin (Invitrogen #R21001). All gRNA sequences are listed in Data S1.

CRISPRa (dCas9-VP64) expression constructs were as follows: EF1a-NLS-dCas9-VP64-2A-Blast-WPRE (Addgene #61425) and pLV-U6-gRNA-UbC-eGFP-P2A-Bsr (Addgene #83925). pLV-U6-gRNA-UbC-eGFP-P2A-Bsr (Addgene #83925) linearized using the BsmBI restriction enzyme (NEB #R0739) at standard conditions. Guide selection, insertion, and verification as outlined above. gRNAs were introduced into human fibroblasts *via* lentiviral infection for a minimum of 48h and GFP expression (typically in >90% of cells) was confirmed prior to introduction of EF1a-NLS-dCas9-VP64-2A-Blast-WPRE (Addgene #61425) *via* lentiviral infection for 48h. All gRNA sequences are listed in Data S1.

To generate the dCas9-KRAB (Y46A) mutant (pLenti-(BB)-EF1a-KRAB-Y46A-dCas9-P2A-BlastR), a fragment of the KRAB domain was PCR amplified from pLenti-(BB)-EF1a-KRAB-dCas9-P2A-BlastR (Addgene #118154) with the following primers: fwd: tcgtgtacagaaatgtgatgctggagaacgctaagaacctg, rev: ttgtacacggtgaagtactcgtacagcaggc. The PCR was performed using Expand High Fidelity PCR System (Roche #0473825001), and the forward primer encoded the mutations which would results in Y46A. The PCR product and template plasmid were subject to restriction digest with BsrGI (NEB #R3575) using standard conditions. The linearized template plasmid and digested PCR product were ligated using T4 DNA Ligase (Thermo Fisher #15224017). The introduction of KRAB Y46A was sequence verified by Nanopore whole-plasmid sequencing (Plasmidsaurus). *FXN*-specific gRNAs used for CRISPRi were cloned into pLenti-(BB)-EF1a-KRAB-Y46A-dCas9-P2A-BlastR as described above. Final constructs were sequence verified by Nanopore whole-plasmid sequencing (Plasmidsaurus). Constructs were introduced to human fibroblasts *via* lentiviral infection for 48 hours followed by 48 hours of selection with Blasticidin. All gRNA sequences are listed in Data S1.

For dCas9-EGFP targeting to the *FXN* locus, three different *FXN*-specific guide oligos were introduced into individual pLenti-SpBsmBI-sgRNA-Hygro (Addgene #62205) by plasmid digestion with BsmBI and ligation using T4 DNA ligase. These were introduced simultaneously with pLenti-dCas9-EGFP-Blast (This study) in human fibroblasts *via* lentiviral infection for 4 days. All gRNA sequences are listed in Data S1.

To generate pLJM1-Smc3, pLJM1 (Addgene #19319) was digested with NheI (NEB R3131) and BamHI (NEB R3136) and the large fragment (hereafter, 'backbone') isolated by agarose gel electrophoresis followed by extraction and purification (QIAquick Gel Extraction Kit #28704). Using pCAGGS-3XFLAG-Smc3-mKate2-bpA (Addgene #156447) as template, Smc3 was amplified and homology arms compatible with Gibson Assembly were introduced by PCR (NEB #M0492). Using pLJM1 as template, additional flanking sequences compatible with Gibson Assembly were generated by PCR (NEB #M0492). The resulting fragments were ligated into the pLJM1 backbone via Gibson Assembly (NEB# E2621) and the reaction transformed into chemically competent *E. coli* (NEB #C3040). Positive clones were identified by Nanopore whole-plasmid sequencing (Plasmidsaurus). Using pLJM1-Smc3 as template, the K38A mutation was introduced into Smc3 to generate pLJM1-Smc3_K38A via PCR (NEB #M0492) site-directed mutagenesis and Gibson Assembly (NEB #E2621). The reaction was then transformed into chemically competent *E. coli* (NEB #C3040) and positive clones were identified by Nanopore whole-plasmid sequencing (Plasmidsaurus).

shRNA-expressing constructs was generated as follows: SGEP (Addgene #111170) or pLKO.1-puro (Addgene #8453) plasmids were subjected to restriction digest with EcoRI (NEB #R0101) and XhoI (NEB #R0146) using standard conditions and shRNA sequences ligated using NEBuilder HiFi DNA Assembly Master Mix (NEB #E2621). Insertions were sequence verified. shRNA targeting CTCF in pLKO.1-puro was generated by the University of Pennsylvania's High Throughput Sequencing Core. shRNA target sequences can be found in Data S1. shRNA-mediated knockdown was achieved through lentiviral infection for 3 days. All shRNA targeting sequences can be found in Data S1.

Lentiviruses were generated in LentiX-HEK293T cells using Lipofectamine 2000 (Invitrogen #11668019) with standard packaging plasmids (Addgene #12260 and Addgene #12259). Virus was supplemented with polybrene (5 μg/ml, Sigma #TR-1003-G) and introduced into human fibroblast, HCT116, and hiPSC cultures using spinocculation by centrifugation at 850xg for 45 minutes at room temperature. Cells were then incubated in virus-containing media overnight at 37°C with 20% O2 and 5% CO2.

RNA isolation, preparation and qRT-PCR

Cells were lifted from culture dishes and centrifuged at 200xg for 5 minutes at 4°C. After discarding the supernatant, pellets were flash frozen on dry ice and stored at -80°C. RNA was isolated using QIAGEN RNeasy total RNA extraction kit (Qiagen #74106) with RNA quality determined using nanodrop. Isolated RNA was converted to complementary DNA (cDNA) using iScript cDNA Synthesis kit

(BioRad #1708891) according to kit instructions. Quantitative RT-PCR (qRT-PCR) was performed in triplicate using PowerUp SYBR Green Master Mix (Thermo Fisher #A25742) with *GAPDH* used as a reference control gene. Data calculated as the fold change (deltadelta Ct method) of treatment versus control samples and is presented as relative gene expression. Primer sequences can be found in Data S1.

Chromatin fractionation

Fibroblast cells were resuspended with lysis buffer (10 mM HEPES pH7.9, 3 mM $MgCl_2$, 5 mM KCl, 140 mM NaCl, 0.1 mM EDTA, 0.5% NP-40, protease inhibitor [Sigma #11836170001]) and incubated for 20 minutes at 4°C. After centrifugation (5,000xg for 5 minutes at 4°C), the supernatant, which contains the cytosol and soluble nucleoplasm fraction, was discarded. The pellet which contains the chromatin fraction was resuspended with benzonase (Sigma #E1014) in the same lysis buffer. After incubation for 45 minutes at 4°C, the chromatin lysate was collected by centrifugation (13,200xg for 20 minutes at 4°C). Following the BCA assay, samples were boiled with sample buffer (NuPAGE LDS Sample Buffer [Invitrogen #NP0007] and NUPAGE reducing reagent [Invitrogen #NP0009]) for 10 minutes and analyzed by immunoblotting as described below.

Immunoblot analysis

Cells were centrifuged at 200xg for 5 minutes at 4°C and pellets were flash frozen in dry ice and stored at -80°C. Lysates were extracted using lysis buffer (10mM HEPES, 3mM $MgCl_2$, 5mM KCl, 140mM NaCl, 0.1mM EDTA, 0.5% NP-40, supplemented with protease inhibitor and 0.5μM DTT) and peptide concentration measurements obtained by BCA Protein Assay Kit (Thermo Fisher #23225). Lysates were run on 4-12% Bolt Bis-Tris protein gels (Invitrogen #NW04122) and transferred onto PVDF membranes. Blots were incubated in blocking solution of 5% milk in 1x Tris-Buffered Saline with 0.1% Tween (1x TBST) for 1 hour at room temperature. Incubation with primary antibodies diluted in blocking solution for 1 hour at room temperature were carried out using the following antibodies and dilutions: anti-Cas9 (1:1000, CST#14697), anti-β-Actin (1:1000, CST#4967), anti-GAPDH (1:1000, CST#2118), anti-FXN (1:800, Abcam #ab175402), anti-GFP (1:1000, Abcam #ab290), anti-RAD21 (1:500, Abcam #ab992), anti-Histone 3 (1:10,000, Abcam #ab1791), anti-CTCF (1:1000, CST#3418), anti-SMC3 (1:500, CST#5696). For analysis of chromatin fractions, the following antibodies and dilutions were used: anti-RBMX (1:1000, CST#14794), anti-RAD21 (1:1000, Millipore #05-908), anti-NIPBL (1:1000, SCBT #sc374625), anti-WAPL (1:1000 SCBT #sc365189), anti-hnRNPL (1:1000, SCBT #sc32317), anti-RBMX (1:1000, CST#14794S). Blots were washed for 1 hour in 1x TBST before incubation with secondary antibodies (1:3000: anti-rabbit HRP-conjugated secondary antibody, CST#7074. Anti-mouse HRP-conjugated secondary antibody, CST#7076) diluted in blocking solution for 1 hour at room temperature. Washing with 1x TBST for 1 hour was repeated before visualization using SuperSignal West Femto Chemiluminescent Substrate (ThermoFisher #PI34095). Molecular weights annotated in supplemental figure immunoblots correspond to the predicted molecular weight reported by the antibody manufacturer or estimated molecular weight determined by validation studies.

Triptolide experiments

For LMNB1 ChIP experiments, RAD21-mAID-HCT116 cells were propagated in standard medium (McCoy's with 10% FBS and 1% penicillin/streptomycin) and plated in 10 cm dishes at 40% density and grown overnight. The following morning, a time course was started for three conditions (DMSO control, triptolide-only, and auxin + triptolide). At time 0, DMSO (Sigma #D2650) control and triptolide-only cells were incubated in fresh media alone; auxin + triptolide cells were incubated in fresh media + 1 μM auxin analog (5-Ph-IAA, MedChemExpress #HY-134653). After 1 hour, 200 nM final triptolide (CST#97539) was added to triptolide-only and auxin analog + triptolide cells. 12 hours post-triptolide, all cells were harvested for ChIP (see "ChIP and library preparation for sequencing"). DMSO was used as a vehicle control.

To confirm transcriptional inhibition by triptolide, RAD21-mAID-HCT116 cells were propagated in standard medium and plated in 12-wells dishes with and without coverslips at 40% density and grown overnight. The following morning, control cells were incubated in fresh media alone and triptolide-only cells were incubated in media + 200 nM triptolide for 12 hours and harvested for qRT-PCR analysis (see "RNA isolation, preparation and qRT-PCR").

OligoFISH probe design and synthesis

All primary probes were designed using OligoMiner pipeline using the default settings.[121] DNA-FISH probes were designed as tiled 80-mers with a density of 4 probes per kb. Probes were designed to hybridize across the entire length of the gene. If genes were smaller then 50 kb, flanking genomic regions were included in the target sequence. For visualization, primary probes were either amplified with direct dye conjugation (Cy5) or introduced along with a fluorescent secondary probe (Alexa 488, Alexa 555, or Alexa 647). Intronic RNA-FISH probes were designed corresponding to the introns on the transcript using 40–45 oligos per transcript. For visualization, fluorescent secondary probes were utilized (Alexa 647). The gene targets and corresponding chromosomal coordinates can be found in Data S1.

ChIP and library preparation for sequencing

Samples for ChIP were processed as previously described.[9] Human NTC and FRDA fibroblasts and RAD21-mAID-HCT116 cells were cultured in 10 cm dishes and crosslinked in culture using methanol-free formaldehyde (Thermo Fisher #28906) for 10 minutes

at room temperature with gentle rotation (final 1% v/v). Crosslinking was quenched by addition of glycine for 5 minutes at room temperature with gentle rotation (final 125 mM). Cells were washed with 1x PBS once before collection *via* scraping and PBS removal by centrifugation (250xg for 5 minutes at room temperature). Resulting pellets were flash frozen on dry ice and stored at -80°C. For each ChIP sample, 30 μL protein G magnetic beads (Invitrogen #10004D) were washed 3 times in blocking buffer (0.5% BSA [Sigma #A4503] in 1x PBS) before beads were resuspended in 250 μL blocking buffer and 2 μg (anti-LaminB1 [Abcam #ab16048], anti-H3K9me2 [Active Motif #39239]) or 4 μg anti-RAD21 (Abcam, #ab992) antibody and rotated at 4°C overnight. Nuclei were isolated from frozen pellets as follows: pellets were resuspended in 10 mL cold Lysis Buffer 1 (50 mM HEPES-KOH pH7.5, 1 mM EDTA, 140 mM NaCl, 10% Glycerol, 0.5% NP-40, 0.25% TritonX-100, and protease inhibitor) and rotated at 4°C for 10 minutes. Resuspended cells were centrifuged at 250xg for 5 minutes at room temperature and supernatant discarded. Remaining pellet was resuspended in 10 mL cold Lysis buffer (220 mM NaCl, 10 mM Tris-HCl pH8.0, 1 mM EDTA, 0.5 mM EGTA, and protease inhibitor) and rotated at 4°C for 10 minutes. Resuspended cells were centrifuged at 250xg for 5 minutes at room temperature and supernatant discarded. Nuclei were resuspended in 1 mL cold Lysis Buffer 3 (10 mM Tris-HCl pH8.0, 100 mM NaCl, 1 mM EDTA, 0.5 mM EGTA, 0.1% Na-Deoxycholate, and protease inhibitor). Samples were transferred to a pre-chilled 1 mL Covaris AFA tube (Covaris #520130) and sonicated using a Covaris S220 sonicator (high cell chromatin shearing for 15 minutes). TrintonX-100 (final 1%) was added to lysates and centrifuged at top speed for 10 minutes at 4°C. Supernatant was collected, and protein concentration measured *via* Bradford assay. Antibody-conjugated beads were washed 3 times in blocking buffer and resuspended in 50 μL blocking buffer before 500 μg protein lysate was added and allowed to rotate overnight at 4°C. For inputs, 50 μg protein lysate was aliquoted and stored at -20°C. The next day, antibody-conjugated beads with lysate were washed 5 times for 2 minutes each at 4°C with rotation in 1mL RIPA buffer (50 mM HEPES-KOH pH7.5, 500 mM LiCl, 1 mM EDTA, 1% NP-40, 0.7% Na-Deoxycholate). Beads were washed in 1 mL Final Wash buffer (1x TE, 50 mM NaCl) for 2 min with rotation at room temperature. Lastly, beads were resuspended in 210 μL Elution Buffer (50 mM Tris-HCl pH8.0, 10 mM EDTA, 1% SDS) and incubated at 65°C for 30 minutes with agitation. 200 μL eluate was removed and all samples were incubated at 65°C with agitation for a minimum of 12 hours, but no more than 18 hours. 200 μL of 1x TE was added the resulting samples followed by addition of RNase (final 0.2 mg/mL, Sigma #10109169001) and incubated at 37°C for 2 hours. Proteinase K was subsequently added (final 0.2 mg/mL, Roche #3115879001) and incubated at 55°C for 2 hours. DNA was isolated via phenol:chloroform extraction and resuspended in 10 mM Tris-HCl pH8.0. DNA was quantified by Qubit.

ChIP-seq libraries were prepared using NEBNext Ultra II DNA library prep kit (NEB #E7770L). Samples were prepared with dual unique indices for multiplex sequencing using NEBNext Multiplex Oligos (NEB #E7630). Library quality was determined by BioAnalyzer or 2% agarose gel electrophoresis and quantified by qPCR using NEBNext Library Quant Kit (NEB #E7630S). Libraries were pooled, re-quantified, and single-end sequenced on the Illumina NextSeq500, NextSeq1000/2000 and Novaseq 6000 platforms.

Immunofluorescence microscopy staining

In preparation for staining, human NTC and FRDA fibroblasts were grown on uncoated coverglass while RAD21-mAID-HCT116, HCT116, and hiPSCs were grown on coated coverglass (0.1% Poly-L-Lysine [Sigma #P8920] or 0.5 mg/mL Matrigel [Sigma #LCS356234], respectively) in appropriate culturing conditions. All the following steps were performed at room temperature. Cells were washed once with 1x dPBS before fixing with 2% paraformaldehyde (Electron Microscopy Sciences #15710) for 10-12 minutes followed by three washes of 5 minutes each with 1x dPBS. Cells were permeabilized by incubation in 0.4% Triton X-100 in 1x dPBS for 15 minutes followed by incubation in blocking solution of 1% Bovine Serum Albumin (Sigma #A4503) in 1x dPBS with 0.05% Tween (1x PBST) for 1 hour. Primary antibodies were then incubated for 1 hour in blocking solution. The antibodies used along with their corresponding dilution ratios are as follows: anti-LaminB1 (1:1000, Abcam #ab16048), anti-H3K9me2 (1:1000, Active Motif #39239), anti-GFP (1:1000, Abcam #ab290), and anti-OCT4 (1:1000, Millipore #MAB4419). After incubation with primary antibody, cells were washed three times with 1x PBST for 5 minutes each before incubation with secondary antibodies diluted in blocking solution for 1 hour (1:2000:Invitrogen #A32731, Invitrogen #A10680, Invitrogen #A32732, or Invitrogen #A32727). Cells were then washed three times with 1x PBST for 5 minutes each before incubation with DAPI (1 ng/mL in 1x dPBS, Sigma #D9542) for 5 minutes. Samples were mounted with SlowFade Fold Antifade Mountant (Invitrogen #S36936) and imaged (see *Image acquisition*).

DNA-FISH and DNA-FISH with immunofluorescence (DNA-FISH and immunoDNA-FISH)

Cells were plated on coverglass as described above. The following protocol was carried out for each cell type with the indicated cell type-specific differences. Cells were washed once with 1x dPBS followed by fixation with 2% PFA with 0.1% Tween20 for 10 minutes at room temperature. Cells were then washed three times for 5 minutes each in 1x dPBS and stored in 0.02% sodium azide (Sigma #S2002) in 1x dPBS at 4°C for at least overnight. Cells were immunostained as described above. Following immunostaining, all remaining steps were performed with samples protected from light. Samples were post-fixed with 2% PFA for 10 minutes at room temperature, followed by three washes for 5 minutes each using 1x dPBS. Samples were then re-permeabilized using 0.7% TritonX-100 for 10 minutes at room temperature, then rinsed with 1x dPBS. RAD21-mAID-HCT116 cells were then incubated in 70% ethanol, 90% ethanol, and 100% ethanol for 2 minutes each. Samples were then incubated in the following solutions for indicated durations and temperatures: 2x SSC (Invitrogen #15557036) with 0.1% Tween (2x SSCT) at room temperature for 5 minutes, 2x SSCT with 50% formamide (Thermo Fisher #BP227500) at room temperature for 5 minutes, 2x SSCT with 50% formamide at 92°C for 5 minutes (for RAD21-mAID-HCT116, 37°C for 1 hour), and 2x SSCT with 50% Formamide at 60°C for 20 minutes. 50-100 pmol primary

DNA-FISH probes diluted in 20 μL hybridization buffer (50% Formamide, 25% Dextran Sulfate [Fisher #BP1585], 10 μg RNAseA, 5 mM dNTPs [Invitrogen #18427088]) were added to each coverslip and heated to 92°C for 5 minutes (for RAD21-mAID-HCT116 and hiPSCs, 80°C for 30 minutes) before overnight incubation at 37°C in humid conditions. After hybridization, samples were washed in 2x SSCT for 15 minutes at 60°C, then for 10 minutes each in 2X SSCT and 2X SSC at room temperature. 10 pmol secondary fluorescent DNA oligo probes were diluted in 20 μL hybridization buffer (10% Formamide, 25x Dextran Sulfate) and added to each coverslip before incubation for 1 hour at room temperature in humid conditions. Samples were then washed for 5 minutes each in 2X SSCT at 60°C, 2x SSC at room temperature, and 2x SSC with DAPI (1 ng/mL in 1x dPBS, Sigma #D9542) at room temperature (for STORM microscopy, DAPI staining was omitted). Samples were briefly rinsed with 1x dPBS and mounted on to glass slides with SlowFade Fold Antifade mountant (Invitrogen #S36936).

RNA-FISH with immunofluorescence (immunoRNA-FISH)

Cells were plated on coverglass as described above. Samples were washed briefly with 1x dPBS before fixation in 4% PFA for 10 minutes at room temperature followed by three washes of 5 minutes each in 1x dPBS. Samples were permeabilized overnight at 4°C in 70% ethanol with 1% SDS. The next day, samples were washed twice briefly with 2x SSCT before addition of 0.03125 μM primary intronic oligo probe diluted in hybridization buffer (25% Dextran Sulfate, 50% Formamide, 1% SDS [Invitrogen #15553027]). Mineral oil was layered on top of the probe-containing hybridization mix to prevent evaporation. Samples were denatured at 60°C for 3 minutes before overnight incubation at 42°C in humid conditions. Samples were briefly washed three times with 2X SSC at room temperature followed by incubation in 2x SSC at 65°C for 20 minutes and 2x SSC at room temperature for 4 minutes. 0.05 μM secondary fluorescent oligo probes diluted in hybridization buffer were added to each coverslip and allowed to incubate at 37°C for 1 hour. Samples were washed with 2x SSC with DAPI (1 ng/mL in 1x dPBS, Sigma #D9542) for at 37°C 5 minutes followed by 2XSSC at 37°C for 5 minutes. For immunoRNA-FISH, samples were then washed with 1x dPBST (1x dPBS with 0.05% Tween20) twice for 5 minutes each at room temperature. Primary antibody (anti-LMNA, 1:1000, SCBT #sc376248) was diluted in blocking buffer (1x dPBS, 3% BSA, 0.1% Tween20, 0.4 U/μL RNase OUT [Invitrogen #1077019]) and samples were incubated for 1 hour at room temperature. Samples we washed three times for 5 minutes each with 1x dPBST at room temperature before fluorescent secondary antibody (1:2000, Invitrogen #A32727) diluted in blocking buffer was added and let incubate for 1 hour at room temperature. Three washes with 1x PBST for 5 minutes each was followed by incubation with DAPI for 5 minutes (1 ng/mL in 1x dPBS, Sigma #D9542) then a brief rinse with 1x PBS and mounting on to glass slides with SlowFade Fold Antifade Mountant (Invitrogen #S36936). Samples were imaged immediately.

Image acquisition

Confocal fluorescence microscopy

All confocal immunofluorescent images were acquired using a Leica SP8 confocal microscope using Leica Application Suite X Software (Version: 3.5.9.29787) and a Leica HC PL APO CS2 63x/NA1.40 oil objective. Microscope is equipped with four lasers: 405 nm, 488 nm, 552 nm and 638 nm and three HyD detectors. For DNA and RNA-FISH, images were acquired in the standard mode with 100% gain and each field of view consisted of 1024x1024 pixels while H3K9me2 imaging consisted of 2048x2048 pixels. For all DNA-FISH and immunoRNA-FISH experiments in this study, individual nuclei were imaged as Z-stacks at 0.120 μm increments with a range of 30–60 planes per nucleus. Channel shift alignment was performed using 0.1 μm TetraSpeck fluorescent beads (Invitrogen #T7279). All nuclei imaged in this study were selected at random. Representative images are planes, therefore, only alleles localized within that plane will be visible. All images are single-plane confocal images except OligoSTORM imaging, unless otherwise indicated.

Stochastic optical reconstruction microscopy

Stochastic Optical Reconstruction Microscopy (STORM) images were performed using a Nanoimager-S 70 (Oxford Nanoimaging) using NimOS NanoimagerTM Software (Version: 1.7.210222-3a3ef15d. Build number: 4. 2016-2019 Oxford Nanoimaging Ltd. All rights reserved). Microscope was equipped with four lasers: 405 nm, 488 nm, 561 nm and 640 nm with 498-551 and 576-620 nm band-pass filters for channel 0 and 666-705 nm band-pass filters for channel 1. A 100x/NA1.4 oil immersion objective (Olympus) was used to collect fluorescence signal and imaged onto a Hamamatsu Flash 4 V3 sCMOS camera with a pixel size of 117 nm and a field of view of 50 μm x 80 μm. HILO (Highly Inclined and Laminated Optical sheet illumination) was used for all imaging sessions. During imaging, all cells in this study were randomly selected. Samples were imaged using a Magnetic imaging chamber (Quorum Tech #CM-S22-1) using freshly prepared STORM imaging buffer (10% [w/v] Glucose, 50 mM Tris pH8.0, 10 mM NaCl, 1% 2-Mercaptoethanol [Bio-rad #1610710]), and 1% Glucose Oxidase Solution (56 mg/mL Glucose Oxidase [Sigma #G2133], 2 mg/mL Catalase [Sigma #C3556] diluted in a buffer of 10 mM Tris pH8.0 and 50 mM NaCl) replaced every 45 minutes. Conventional fluorescence images for anti-LMNB1 and DNA-FISH were acquired for each field of view prior to STORM imaging. During STORM image acquisition, each field of view was simultaneously illuminated with 405 nm and 647 nm illumination with 15 ms exposure for 30,000 frames each.

QUANTIFICATION AND STATISTICAL ANALYSIS

Microscopy analysis

Locus radial positioning and probe center-center distance

Confocal 3D images were deconvolved using Leica Lightning Process Deconvolution (Version 3.5.6.21594) using automatic settings based on coverglass thickness, mountant refractive index, and pinhole size during image acquisition. Representative images show a single focal plane unless noted otherwise. For distance from the lamina measurements, 3D reconstructions were generated using Imaris v8.1.2 software (Bitplane AG, Switzerland). The nuclear lamina was generated using the Surfaces tool on fluorescent signals from anti-LMNB1 antibodies and using automatic settings. DNA or RNA-FISH dots were generated using the Spots tool using a 300 nm diameter from fluorescent signals from oligo probes. Distance from the center of the FISH spot to the center of the lamina was measured in three dimensions using the Measurements tool.

To measure the distance between the center of DNA-FISH probe pairs, 3D reconstructions of each dot was generated using the Spots tool using a 300 nm diameter from fluorescent signals from each oligo probe. Using the Measurements tool, the distance between the center of one spot to the center of another spot was measured. For each FISH experiment performed in this study, data represents measurements from at least two biological replicates and equal to or greater than 50 nuclei per condition, unless otherwise stated.

H3K9me2 thickness

Confocal 3D images were deconvolved as described above. Representative images show a single focal plane. 3D reconstructions were generated with Imaris v8.1.2 software (Bitplane AG, Switzerland) using the Surfaces tool with automatic settings based on the fluorescent signal from anti-H3K9me2 antibodies. To calculate H3K9me2 thickness, the Measurements tool was used to measure the distance from the inside surface to the outer surface of the H3K9me2 surface. For each condition in this study, 10 independent nuclei were acquired and five measurements from each were taken at different regions around the nuclei circumference resulting in 50 measurements per condition. For the *FXN*-CRISPRi experiments, H3K9me2 thickness was not significantly different between dCas9-KRAB introduction with a scramble guide versus the *FXN*-specific guides, therefore the collective measurements from all three conditions were pooled and the 90th percentile value was used as the H3K9me2 thickness. For all other experiments performed, the H3K9me2 thickness used was the 90th percentile value from experimental control nuclei.

DNA-FISH probe volume

Deconvolved confocal 3D images, as described above, were segmented based on the fluorescent signal from the oligo probes and volume was measured using a modified version of TANGO 3D-segmentation plug-in for ImageJ/Fiji as previously described.[53]

STORM

Images were analyzed using custom-written Matlab codes using MatLab R2020a and all mages were drift-corrected post-acquisition (Nanoimager sotware, Oxford Nanoimaging). STORM bin files were overlapped with the corresponding conventional fluorescent images to manually crop the region of interest containing the DNA-FISH signal. Bin files were then used for cluster localization by Voronoi segmentation based on a minimum of 500 localizations per cluster/puncta. The degree of compaction was determined by the radius of gyration, ßcalculated as the root-mean square distance of localization positions from their centroid position, similar to.[77,122] Representative Gaussian renderings were generated from isolated clusters and heatmap density renderings were generated using Voronoi-Area Density Maps in MatLab.

Genomic analyses

ChIP-seq analysis

Raw base calls were demultiplexed with bcl2fastq v2.20 (Illumina, San Diego, CA) based on the indexes used during the library preparation. ChIP-seq single-end reads were quality controlled using FastQC (v0.12.1).[123] Adapter trimming, read de-duplication, and low complexity filtering was performed using fastp (v0.23.2).[124] Processed reads (target $\geq$ 30 million per library) of 120 bp were aligned to the human reference genome (GRCh38.p13) using Bowtie2 (v2.5.1) with default parameters.[125] Reads mapping with MAPQ > 20 to chr 1 to 22, X and Y were retained and deduplicated using Sambamba (v1.0.0)[126] with the filter string 'mapping_quality>=20 and ref_name =~ / ^chr[0-9XY]/ and not duplicate'. To mitigate read biases, the bam files containing the filtered aligned reads were down-sampled to match the library with the fewest mapped reads per condition using SAMtools (1.16.1)[127] 'samtools view -b -s'. All ChIP-seq experiments were performed in biological duplicates for every antibody–condition pair – input, LMNB1, and RAD21 across NTC, scr-CRISPRi, *FXN*-CRISPRi, and FRDA in fibroblasts; and vehicle-, triptolide-, and triptolide + auxin-treated HCT116 – except the H3K9me2 samples (n = 1) and the LMNB1 HCT116 samples (n = 3). genome-wide Spearman correlations between replicates were computed with deepTools (v3.5.1)[128] using 500 kb bins with all duplicate and triplicate pairs achieving $\rho > 0.9$. Upon confirming high concordance, replicates were merged into a single, high-coverage dataset per antibody and condition for all downstream analyses.

ChIP-seq coverage tracks and peak calls

Coverage tracks for pooled condition-antibody datasets were generated by first extending the reads to 120bp, scaling the libraries to counts per million (CPM) and normalizing them to their corresponding input libraries. Blacklisted regions (https://github.com/Boyle-Lab/Blacklist/tree/master/lists) were excluded from subsequent analyses at this stage.[129] For broad domains (LMNB1 & H3K9me2), enrichment over input was calculated using log2 rations in 1kb across the genome using bamCoverage and bamCompare from

deepTools.Track visualization was performed using pyGenomeTracks (v3.8)[130] after calculating the sliding average signal across a 10-bin window. Regions of enrichment were identified based on a 2-state Hidden-Markov Model using HMMDomainCaller as previously published[131] with few modifications (https://github.com/rikrdo89/HMM_caller). We used BEDtools (v2.30.0),[132] bedops (v2.4.41),[133] eulerR (v7.0.2),[134] and Intervene (v0.6.5)[135] to evaluate and demonstrate a high degree of overlap between our LAD calls and published LAD calls from LMNB1 DamID-seq (4DN accession: 4DNESXZ4FW4T, vanSteensel lab)[136,137] in human fibroblast cells (HFFc6). All H3K9me2 and LMNB1 ChIP-seq tracks are displayed as log2 transformed tracks of enrichment over input - $\log_2$ (ChIP/Input) - unless otherwise noted. For narrow peaks (RAD21), ChIP-seq coverage tracks were calculated by using the 'bdgcmp' option of MACS2 (v2.2.6)[138] with the 'FE' (fold-enrichment) method by normalizing the ChIP bam files over the corresponding input controls. Peaks were called using MACS2[138] with the significance cut-off q-value <=0.01 and the following parameters '—nomodel—shift 0—extsize 100'.

ChIP-seq signal analyses

ChIP-seq signal profiles for LMNB1 and H3K9me2 were generated genome-wide over their corresponding enriched regions with deepTools 'computeMatrix scale-regions' and then visualized the aggregate profiles with 'plotProfile' using the mean normalized signal. As a background control, we generated an equivalent number of random regions matched for size and chromosome using shuffleBed from BEDtools, computed their mean signal in the same way, and overlaid both observed and shuffled signals as line plots.

Locus-specific LMNB1 ChIP-seq signal – at the *FXN* (Chr 9: 69 030 000–69 079 000) and *TJP2* (Chr 9: 69 121 000–69 274 000) loci – was quantified using two complementary approaches.

1) Subsampling bootstrap for background estimation: We summarized the $\log_2$(Input)-normalized ChIP–seq signal over each entire locus with deepTools multiBigwigSummary (whole-region mode). To model background, 10000 random regions per locus—matched for length, GC content, and mappability—were generated with BEDtools shuffleBed, excluding hg38 blacklist intervals from the Boyle-Lab repository. These 10000 background values were uniformly shuffled and divided into ten non-overlapping blocks of 1000 observations each (m-out-of-n subsampling). The mean signal of each block acted as a pseudo-replicate, producing an empirical background distribution of ten values per locus. We calculated the delta enrichment for each locus as the difference between its observed mean signal and the mean of its background pseudo-replicates, and visualized the distributions in R (v4.3.2)[139] using the ggplot2 (v3.4.4)[140] package.
2) Bin-wise paired comparison across conditions: Each locus was divided into 1 kb bins via deepTools multiBigwigSummary bins. For each bin, we extracted the $\log_2$(Input)-normalized LMNB1 signal under two conditions (e.g., WT vs FRDA or Scr-CRISPRi vs FXN-CRISPRi). Treating each bin as a matched pair, we assessed shifts in signal distributions with a paired Wilcoxon signed-rank test in R using 'ggpubr::stat_compare_means(method="wilcox.test", paired=TRUE, ref.group="WT")'. To assess the magnitude of pairwise differences, we computed the effect size (r) for the Wilcoxon signed-rank test using the wilcox_effsize() function from the rstatix R package. This nonparametric effect size is derived by dividing the Wilcoxon Z statistic by the square root of the number of observations ($r = Z / \sqrt{N}$), providing a standardized measure of effect independent of sample size. Effect sizes were interpreted according to conventional thresholds: small ($r = 0.1$), medium ($r = 0.3$), and large ($r \geq 0.5$).

To quantify global changes in ChIP–seq signal across conditions in the transcription inhibition experiments (vehicle, triptolide, triptolide + auxin), we resource generated genome-wide coverage matrices using deepTools v3.5.1 fin reference-point mode, with each window treated as centered on its midpoint. This produced a tabular matrix of normalized scores per condition for each of the indicated set of regions. We next employed the dsCompareCurves utility (v1.2.0) utility to compare signal distributions across conditions. For each bin, paired Wilcoxon signed-rank tests were applied (threshold $p < 0.05$) to identify significant changes in occupancy between treatments. To estimate the robustness of these differences, 1000 bootstrap resamples of the paired differences were generated, and 95% confidence intervals around the mean difference curve were computed. Windows passing the Wilcoxon significance cutoff were flagged as differentially occupied. The resulting mean difference profiles and confidence bands were plotted in R (v4.3.2) using ggplot2 (v3.4.4).

LAD boundary analysis

LMNB1-enriched domains were delineated in vehicle-treated RAD21-mAID-HCT116 cells by applying a two-state hidden Markov model (HMM) to LMNB1 ChIP–seq signal, as described earlier, yielding 3052 total boundaries. To quantify boundary integrity under transcriptional inhibition, we computed the mean normalized LMNB1 signal in a 50 kb window immediately outside each domain using deepTools computeMatrix reference-point. For each boundary, we compared the mean signal across three biological replicates per condition - vehicle, triptolide, and triptolide + auxin - using a two-sided t-test. Triptolide-sensitive boundaries ($n = 1152$) were defined as those exhibiting a statistically significant increase in mean LMNB1 signal ($p < 0.05$) in the 50 kb window upon triptolide treatment relative to vehicle, indicating LMNB1 spreading across the boundary. Among the triptolide-sensitive set, boundaries showing a significant reduction in mean signal ($p < 0.05$) in the same window upon auxin-mediated RAD21 degradation were defined as RAD21-dependent boundaries ($n = 471$), reflecting restoration of boundary function. Signal enrichment plots display the right-flank windows, with equivalent behavior observed on left-flank boundaries. Gene ontology analysis performed using Toppgene (ToppFUN, default parameters, accessed May 17, 2025).

Analysis of gene expression levels

To assess the baseline expression levels of *FXN*, *C9orf72*, *ZNHIT6*, *HS1BP3*, *GNB2*, and *MRPL43* across different human tissues, we used the RNA consensus gene data from the Human Protein Atlas (https://www.proteinatlas.org/download/rna_tissue_consensus.tsv.zip).[46] The normalized transcripts per million (TPM) values were $\log_2$-transformed and z-normalized across all the tissues, and these values were used to generate a heatmap plot in R using ComplexHeatmap (v2.20.0).[141,142] We also assessed the normal distribution of gene expression levels in human fibroblasts (HFFc6) using the publicly available RNA-seq data from the 4DN data portal (accession 4DNESFH3EHTU, Yue lab).[136,137] The distribution of expression was performed using the $\log_2$ of the average TPM across 2 replicates using geom_histogram from the ggplot2 package in R.

Analysis of publicly available genomic datasets

Genome-wide chromatin interactions in human fibroblasts (HFFc6) were assessed using available Hi-C and Micro-C data from the 4DN data portal. The accession numbers for the experiment sets used are 4DNESWST3UBH[143] for Micro-C and 4DNESN49VY8X[144] for Hi-C, and they include normalized contact matrices, insulation score, compartment and boundaries coordinates, all of which were visualized using pyGenomeTracks (v3.8).[130] Public Hi-C data from HCT116 treated with vehicle or actinomycin D (GSE279166) were used to assess boundary integrity to complement our triptolide experiments in HCT116 cells. Using Coolpup (v0.8.0)[145] in local mode, we centered on each of our previously identified LMNB1 boundary categories (triptolide sensitive, triptolide insensitive, RAD21 dependent) and averaged contacts within ± 250 kb windows. Interactions were normalized to genome-wide expected values and corrected with random-shift controls, yielding aggregate pileup matrices for each category. Differential pileup comparisons between actinomycin D and vehicle were performed using Coolpup's dividepups.py, which computes the element–wise ratio of both aggregate matrices generating a ''delta'' heatmap. All matrices were pre-normalized to expected interaction levels and corrected with random-shift controls prior to division. LMNB1 DamID-seq datasets for human fibroblast HFFc6 (4DNESXZ4FW4T) and HCT116 (4DNES24XA7U8) with at least 2 replicates were obtained from the 4DN data portal. The corresponding normalized signal and LAD calls were downloaded as bigwigs and bed files respectively. ATAC-seq in HFFc6 (4DNESMBA9T3L) was retrieved as processed bigBed and bigWig files. Track visualization, signal profiles, and comparisons for these datasets were performed using the same pipelines and parameters described above to ensure consistency with the experiments in this study.

QUANTIFICATION AND STATISTICAL ANALYSIS

Statistical analyses were performed using Prism 10 software by GraphPad (Version 10.2.0) and R v4.3.2. For each experiment, the data were assessed for normality of distribution by Shapiro-Wilk test and homogeneity of variances by Levene's test (https://www.statskingdom.com/230var_levenes.html). Datasets displaying normal distributions were subjected to unpaired, two-tailed student's t-test or an unpaired t-test with a Welch correction for two groups, and one-way ANOVA or Welch's ANOVA with Dunnett's multiple comparisons test for more than two groups. Datasets that did not follow a normal distribution, were analyzed using an unpaired Mann-Whitney test or Kolmogorov-Smirnov test for two groups and a Kruskal-Wallis test with Dunn's multiple comparisons test for more than two groups. The type of statistical test applied to each dataset is specified in the figure legends. P-values are as follows: ''ns'' >0.05, ''*'' <0.05, ''**'' <0.005, ''***'' <0.0005. Exact p-values can be found in Table S2.